Characterizing the tropospheric water vapor spatial variation and trend using 2007-2018 COSMIC radio occultation and ECMWF reanalysis data

5 Xi Shao[1], Shu-Peng Ho[2], Xin Jing[1], Xinjia Zhou[3], Yong Chen[2], Tung-Chang Liu[1], Bin Zhang[1], Jun Dong[1]

[1]Cooperative Institute for Satellite Earth System Studies (CISESS), Earth System Science Interdisciplinary Center, University of Maryland, College Park, MD, 20740, USA
[2]NOAA National Environmental Satellite, Data, and Information Service, Center for Satellite Applications and Research, College Park, MD, 20740, USA
10 [3]Global Science & Technology, Inc., 7855 Walker Drive, Suite 200, Greenbelt, MD 20770, USA

Correspondence to: Xi Shao (xshao@umd.edu)

Abstract. Atmospheric water vapor is essential in the global energy balance, hydrological cycle, and climate system. High-quality and consistent water vapor data from different sources are critical for numerical weather prediction and climate studies. This study evaluates the consistencies between Formosa Satellite Mission 3–Constellation Observing System for Meteorology,
15 Ionosphere, and Climate (FORMOSAT-3/COSMIC) radio occultation (RO) and European Centre for Medium-Range Weather Forecasts (ECMWF) ReAnalysis Model 5 (ERA5) water vapor datasets. The COSMIC and ERA5 water vapor data at lower (850 hPa), mid- (500 hPa), and upper troposphere (300 hPa) from 2007 to 2018 are compared. These two water vapor datasets generally show good agreements in space and time. At 500 and 850 hPa, COSMIC water vapor retrieval is lower than water vapor from ERA5 globally, with asymmetric latitudinal variability between the southern and northern hemispheres. The water
20 vapor increases around 2015-2016 due to the El Niño event are identifiable in both COSMIC and ERA5 water vapor time-series data. COSMIC global water vapor increasing trends are 3.47±1.77, 3.25±1.25, and 2.03±0.65%/Decade at 300, 500, and 850 hPa, respectively. COSMIC's increasing water vapor trends at 500 and 850 hPa are ~0.8 %/Decade lower than ERA5. Large regional water vapor trend variabilities with strong increasing and decreasing slopes are observed in the tropical and subtropical regions. At 500 and 850 hPa, strong water vapor increasing trends in the equatorial Pacific Ocean and the Laccadive
25 Sea and decreasing trends in the Indo-Pacific Ocean region and the Arabian Sea are recognizable. This study also found that the water vapor increasing trends at 850 hPa estimated from COSMIC are significantly higher than ERA5 data for two low-height stratocumulus cloud-rich ocean regions to the west of Africa and the west of South America. Over land, significant water vapor increasing trends at 850 hPa are found around the southern United States, and decreasing trends are observed in the south of Africa and Australia. The differences between the water vapor trends of COSMIC and ERA5 are primarily negative
30 in the tropical regions at 850 hPa. At 500 hPa, the negative differences between COSMIC and ERA5 trends are mainly distributed in the Indo-Pacific Ocean region. In contrast, the positive differences are in the northern Indian Ocean and its northern coast. These regions with notable water vapor trend differences are located in the Intertropical Convergence Zone

(ITCZ) area with frequent occurrences of convection, such as deep clouds. The difference in characterizing water vapor distribution between RO and ERA5 in a deep cloud may cause such trend differences. Quantitative evaluation of the spatiotemporal variabilities of atmospheric water vapor data helps to assure the qualities of RO-derived and reanalysis water vapor datasets for climate studies.

1. Introduction

Water vapor is one of the most important greenhouse gases in the atmosphere, which accounts for about 60% of the natural greenhouse effect (Kiehl and Trenberth, 1997; Wagner et al., 2006; Foster et al., 2007; Ahrens and Samson, 2011). Water vapor cycles latent heat through condensation and evaporation and is closely linked to clouds and energy budgets, including the radiation balances. In addition, studies showed that water vapor amplifies global warming (Smith and Reynolds, 2005; Parker et al., 2007; Dai, 2006; Allan and Soden, 2008; Mieruch et al., 2008; Zhang et al., 2013). As the earth warms, the water vapor concentration in the lower troposphere increases with increasing temperature, which can further drive both the evaporation rate and the atmospheric water vapor amount to increase and further warm the air. The water vapor's heat-trapping effect is crucial in climate change (Forster et al., 2007). Water vapor profoundly impacts atmospheric temperature structure and hydrological cycle, increasing the likelihood of extreme regional precipitation events, extreme weather conditions, and droughts (Foster et al., 2007; Allan et al., 2010; Trenberth, 2011; Hegerl et al., 2015).

Long-term accurate and consistent atmospheric water vapor climate data records (CDRs) are critical for detecting climate changes, understanding their feedback in the troposphere and stratosphere, and making climate predictions. Various studies have quantified the spatial and temporal variation and trend in atmospheric water vapor using two types of water vapor data: i) measurements or retrievals from sensor observations and ii) reanalysis data produced by assimilating various observations. The first data type includes both ground-based in situ and space-borne observations: long-term radiosonde measurements (Zhai and Eskridge, 1997; Ross and Elliott, 2001; Ho et al., 2010; Zhao et al., 2012; Zhang et al., 2018), weather station data (Dai, 2006), water vapor retrieved from ground-based Global Positioning System (GPS) station data (Kursinski et al., 1997; Bock et al., 2007; Nilsson and Elgered, 2008; Vey et al., 2010; Huang et al., 2013; Chen and Liu, 2016; Yuan et al., 2021), water vapor retrievals from space-borne radio occultation observations (Ho et al., 2009; Huang et al., 2013; Ho et al., 2018; Zhang et al. 2018; Andrisaniand and Vespe, 2020; Gleisner et al., 2022), visible spectral-range sensor observations (Mieruch et al. 2008; Grossi et al., 2015; Borger et al., 2021), and microwave (Rosenkranz, 2001; Chen and Liu, 2016; Ho et al., 2018; Yadav et al., 2021) and infrared sounder observations (Susskind et al., 2003).

The global atmospheric reanalysis products are mainly from the global operational NWP centers such as the European Centre for Medium-Range Weather Forecasts (ECMWF) (Hersbach et al., 2020), the National Centers for Environmental Prediction (NCEP) (Whitaker et al., 2008), and others. These reanalysis data are continuously constructed from assimilating various in

65 situ and satellite observations. These atmospheric reanalysis data have been used in long-term atmospheric water vapor monitoring (Bengtsson, 2004; Wagner et al., 2006; Adler et al., 2008; Ho et al., 2009; Dessler and Davis, 2010; Huang et al., 2013; Zhang et al., 2013; Chen and Liu, 2016; Xie et al., 2020; He et al., 2022) and climate change studies (Allan, 2002; Allan et al., 2014; Lu et al., 2015). However, the performance and quality of the reanalysis data may be affected by i) discontinuity or changes of in situ data and satellite data, ii) the inadequate spatial and temporal coverage of the observations, iii) inadequate

70 measurement bias corrections, iv) preliminary observation error estimates, v) contaminations of ground-based and space-borne satellite observations due to clouds, and vi) potential/unknown model errors (Sherwood et al., 2010; Chen and Liu, 2016). The uncertainty of forecast and reanalysis data under cloudy conditions, especially over oceans, is still very large (Lonitz and Geer 2017) due to not enough drizzle or cloud water in reanalysis compared to observations.

75 Past climate modeling studies suggest that increasing surface temperature can result in an increasing trend in global water vapor (Held and Soden, 2000, 2006; Santer et al., 2006). Studies based on various types of observations and reanalysis data have shown an increasing water vapor trend over different periods ranging from several decades to the recent decade (Bengtsson, 2004; Wagner et al., 2006; Ho et al., 2009; Chen and Liu, 2016; Wang et al., 2017; Ho et al., 2018). However, these studies also showed substantial variation in regional water vapor trends (Ross and Elliott, 2001; Dai, 2006; Mieruch et

80 al., 2008, 2014; Zhang et al., 2018). This is mainly because regional water vapor concentration changes highly depend on multiple non-thermodynamic factors such as i) surface type, ii) long-range transport of air masses, and iii) water availability. As a result, the local surface temperature increase may not necessarily cause the rise of local water vapor (Chou and Neelin, 2004; Wagner et al., 2006; Lu et al., 2015; Chen and Liu, 2016).

85 There have also been efforts to inter-compare water vapor data from global reanalysis with sensor observations and understand their consistencies and differences (Ho et al., 2009; Chen and Liu, 2016; Ho et al., 2018). Chen and Liu (2016) evaluated the global precipitable water vapor (PWV) variability and trend from ECMWF and NCEP reanalysis results. They compared the reanalysis data with 36-year (1979 to 2014) water vapor data from radiosonde, ground-based Global Navigation Satellite System (GNSS), and microwave satellite observations. All five datasets found increasing trends

90 in the global PWV. ECMWF interim reanalysis data agrees with microwave satellite observations better than reanalysis from NCEP. The ECMWF reanalysis overestimates the PWV trend over the ocean for the period before 1992 compared to other sensor data. It is essential to continue comparing the differences and consistencies of atmospheric water vapor data's temporal and spatial variabilities from different sources and assure the climate community with high-quality water vapor data.

95 There is growing interest in comparing reanalysis data and all-weather water vapor profiles retrieved from GNSS radio occultation (RO) (Anthes et al., 2000; Kursinski et al., 2001; Ho et al., 2009, 2010). Complementing the measurements from microwave and infrared sounders, RO data can provide information on the temperature, water vapor, and pressure with high accuracy, precision, and vertical resolution. Because the quality of RO data does not change during the day or night and is not

affected by clouds (Anthes et al. 2008; Ho et al. 2020a), the RO temperature and water vapor profiles co-located with reanalysis

100 data would help identify the variation of temperature and humidity under all-weather conditions over time. RO data has been used to evaluate biases and monitor calibration changes for the measurements of microwaves (Iacovazzi et., 2020; Shao et al., 2021a) and infrared sounders (Chen et al., 2022). RO-derived water vapor profiles have been used to distinguish systematic water vapor biases in radiosondes (Ho et al., 2010; Sun et al. l., 2019; Ho et al., 2020a; Shao et al., 2021b).

105 In this paper, we characterize the water vapor data derived from Formosa Satellite Mission 3–Constellation Observing System for Meteorology, Ionosphere, and Climate (FORMOSAT-3/COSMIC) (hereafter COSMIC) and those from ECMWF Re-Analysis model 5 (ERA5). Launched in 2006, COSMIC was the first constellation of microsatellites carrying GPS RO receivers. COSMIC has demonstrated the value of RO data in the ionosphere, climate, meteorological research, and operational weather forecasting (Ho et al., 2020a). This paper aims to characterize and compare the global, latitudinal, and regional

110 variabilities of COSMIC and ERA5 water vapor distribution, and the seasonality and long-term trends at selected pressure levels from 2007 to 2018. In addition, this paper identifies regions with notable increasing and decreasing water vapor trends, i.e., regions becoming wetter or drier, and regions with significant water vapor trend differences between COSMIC and ERA5. Particular interest is also placed on comparing the COSMIC and ERA5 water vapor trends over the stratocumulus cloud-rich regions to investigate the impacts of stratocumulus clouds on near-surface water vapor data quality in ERA5.

115

This paper is organized as follows: Section 2 introduces the water vapor data from COSMIC RO retrieval and ERA5 reanalysis. Section 3 analyzes global and latitudinal variabilities of long-term (2007-2018) COSMIC and ERA5 water vapor data at three pressure levels, and their differences are quantified. In Section 4, the global and latitudinal water vapor trends derived from COSMIC and ERA5 are quantified and compared at different pressure levels. Section 5 examines the COSMIC and ERA5

120 time series at sites with frequent stratocumulus cloud coverage, notable increasing and decreasing water vapor trends, and large differences between COSMIC and ERA5. As supplementary, the seasonal variability of latitudinal water vapor distribution is summarized in Appendix with the introduction to estimating the water vapor trend with sampling error removal and its associated uncertainties for a given region of interest (RoI). We present the conclusions and discussions in Section 6.

2. Datasets used for Spatial and Temporal Water Vapor Variability Analysis

125 **2.1 ECMWF Reanalysis Data**

This study used the ERA5 global atmospheric and climate reanalysis dataset (https://www.ecmwf.int/en/forecasts/dataset/ecmwf-reanalysis-v5). ERA5 is the fifth-generation ECMWF reanalysis dataset covering the past 4 to 7 decades. The ERA5 dataset is generated from the Four-Dimensional Variational (4DVAR) data assimilation system, which uses a fixed version of the ECMWF NWP system, i.e., Integrated Forecasting System (IFS) Cy41r2.

130 The IFS-Cy41r2 system became operational in 2016 (Hersbach et al., 2020) and blends or assimilates meteorological

observations (e.g., surface weather stations, ocean buoys, radiosonde stations, aircraft, and remote sensing satellites) with a previous forecast to obtain the best for both. These blended results serve as the initial conditions for the next forecast period. The ERA5 water vapor data are from the ground to ~0.1 hPa at 37 mandatory pressure levels. Our study used ERA5 global water vapor profiles from 2007 to 2018 in 6-hour increments. The ERA5 data were collected with a 0.2° spatially gridded resolution, equivalent to a spatial resolution of ~20 km at the equator.

2.2 COSMIC WETPrf water vapor retrieval

The COSMIC RO receivers on the Low Earth Orbit (LEO) satellites measure the phase delay of radio waves, which are emitted from the GPS satellites and occulted by the Earth's atmosphere. Profiles of atmospheric refractivity can be derived from the bending angles of radio wave trajectories when propagating through the ionosphere, stratosphere, and troposphere. The retrievals of RO limb-sounding data first derive bending angle and refractivity profiles from the excess phase data processed from the Doppler-shifted raw radio signals transmitted by GPS satellites. Then, the One-Dimensional Variational (1DVAR) retrieval algorithm is applied to solve an under-determined problem: determine the atmospheric temperature and water vapor profiles from bending angle or refractivity data. The 1DVAR retrieval generally uses *a priori* state of the atmosphere, i.e., vertical background temperature and humidity profile, and associated background and observation uncertainties/error covariance matrices (ECM) to minimize a quadratic cost function.

In this paper, we analyze the 2007 to 1028 COSMIC wet profile data produced by University Corporation for Atmospheric Research (UCAR) from COSMIC RO data, namely WETPrf (https://cdaac-www.cosmic.ucar.edu/cdaac/products.html). The WETPrf data from the COSMIC Data Analysis and Archive Center (CDAAC) consist of temperature, water vapor, and pressure profiles with a high vertical resolution (100 m). UCAR WETPrf profile data contain the latitude and longitude of the RO perigee point, temperature, pressure, water vapor profile, and mean sea level height. COSMIC has provided more than seven million RO-sounding profiles over its lifetime. Many of the six COSMIC GPS receivers continued beyond their 2-year designed life and provided more than 1000 soundings per day through 2016. The COSMIC data decreased significantly in late 2019 and was decommissioned in May 2020.

The UCAR COSMIC WETPrf data was generated with the heritage 1DVAR algorithm at CDAAC to produce wet temperature and humidity profile data. In the 1DVAR algorithm for WETPrf, background profiles are taken from ERA-Interim gridded low-resolution data and interpolated to the time and location of RO measurements to separate the pressure, temperature, and moisture contributions to the refractivity. The constraint applied to WETPrf in the 1DVAR retrieval is very tight, such that temperature and moisture profiles are reported only when the residual refractivity (i.e., the difference between the observed refractivity and simulated refractivity computed from the retrieved temperature and moisture profiles) are within the uncertainty of refractivity. This ensures that the information on refractivity measurements from RO is completely used in the 1DVAR (Ho et al., 2020a).

165   In our analysis, COSMIC RO profiles with the 'Bad' flag have been filtered out. COSMIC RO and ERA5 water vapor profiles are paired through collocation before the study. The ERA5 data have a global distribution over 0.2-degree latitude/longitude grids, vertically over 37 pressure layers, and at 6-hour intervals. Therefore, the ERA5 water vapor data at a given pressure level are interpolated at the latitude/longitude of the perigee point of the RO profile and at RO time to match the COSMIC RO measurement. For RO data, the fine vertical resolution COSMIC RO water vapor profiles are interpolated onto three pressure

170   levels, e.g., 300, 500, and 850 hPa, selected to characterize water vapor variations at representative heights around 9 km, 5.5 km, and 1.5 km, respectively. In particular, the pressure level at 850 hPa is close to the surface, and the COSMIC water vapor retrieval is strongly affected by super-refraction in the moisture-rich regions (Ho et al., 2010). The retrieved water vapor at 850 hPa from COSMIC data could differ from ERA5, making it worth evaluating the relative biases and consistency in the trends between these two datasets. Starting from the pressure level at 500 hPa, the RO-water vapor retrieval uncertainty

175   increases as height decreases. The 300 hPa pressure level represents the water vapor with fewer horizontal variations at higher heights.

    The UCAR's 1DVAR retrieval algorithm for COSMIC WETPrf (water vapor and humidity) uses ERA-Interim profiles as the *a priori* input (Wee et al., 2022). In addition, the UCAR WETPrf water vapor/temperature retrieval also enforces a retrieval

180   constraint to the residual refractivity. Such a constraint can determine the influence of ERA-Interim on the final water vapor retrieval at different pressure levels. On the other hand, the ERA5 provides a more comprehensive and reliable reanalysis by using improved weather forecast and data assimilation models with various ground, in-situ, and satellite measurements compared to ERA-Interim (Fujiwara et al., 2017; Hersbach et al., 2020). Figure 1 depicts the monthly (using January and July of 2007 as representative winter and summer months of the northern hemisphere) scatter plots of the collocated COSMIC

185   global water vapor versus ERA5 and ERA-Interim water vapor data at three pressure levels. The linear regression statistics for COSMIC versus ERA5 and COSMIC versus ERA-Interim comparisons are also shown on the plots. All plots show that COSMIC versus ERA-Interim comparisons are more scattered than the COSMIC versus ERA5 comparison. Quantitatively, the correlation coefficients between COSMIC and ERA5 are around 0.96, while the correlation coefficient between COSMIC and ERA-Interim varies from 0.88 to 0.93. The linear fitting coefficients, i.e., slopes, of COSMIC versus ERA5 fittings are

190   closer to 1 than COSMIC versus ERA-Interim fitting in all panels of Figure 1. In terms of the linear fitting root-mean-square-error (RMSE) residuals, the RMSEs of COSMIC versus ERA5 fitting are lower than the COSMIC versus ERA-Interim fitting by 24% to 47% over the two selected months (January and July of 2007) and three pressure levels. These analysis results indicate that the COSMIC water vapor retrievals are more consistent with ERA5 than ERA-Interim. It suggests that the information on COSMIC 1DVAR retrievals is mainly from the COSMIC refractivity instead of the ERA-Interim.
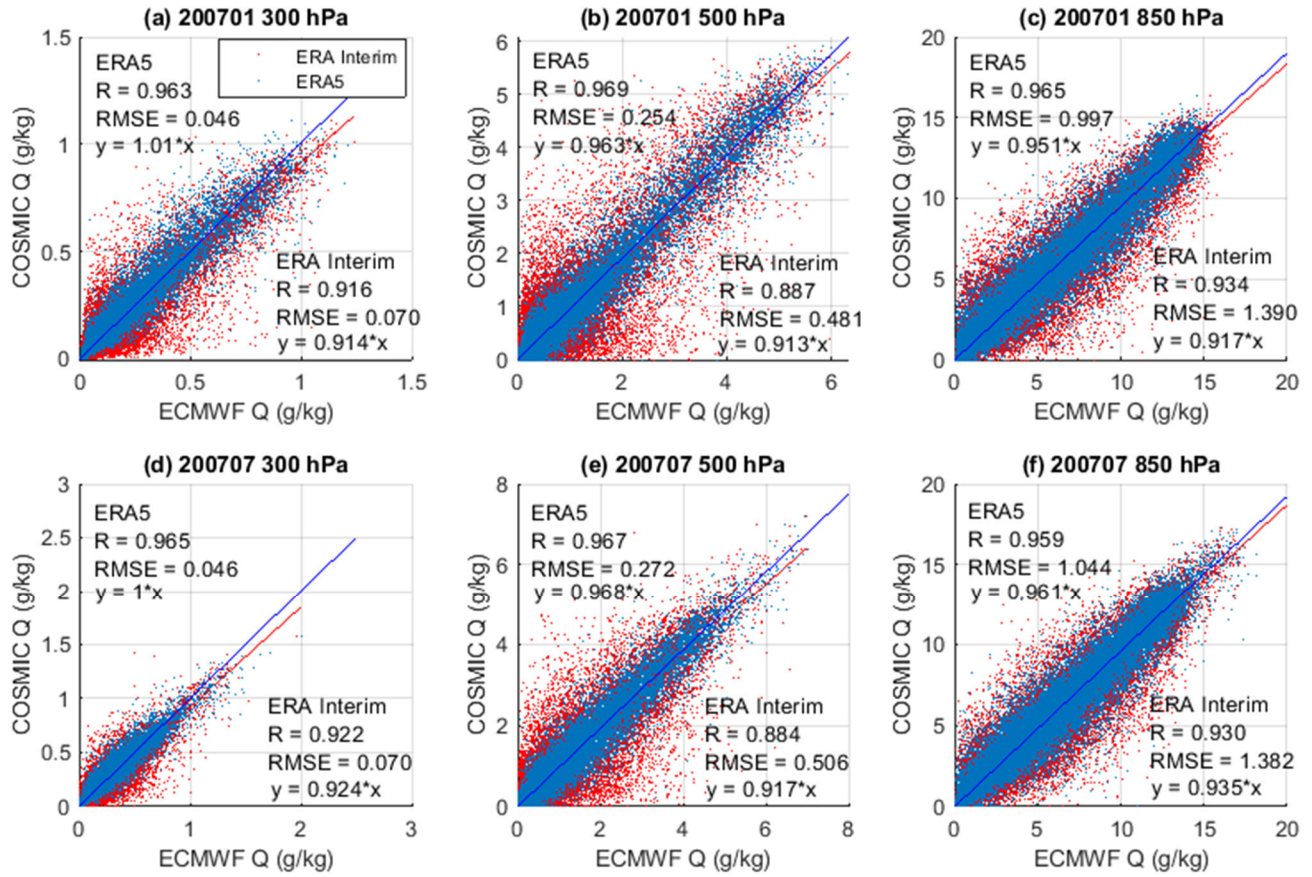
195

Figure 1: Scatter plots of collocated COSMIC water vapor retrieval versus ERA5 and ERA-Interim water vapor data for two months (a, b, c: 2007/01; d, e, f: 2007/07) at three pressure levels: (a, d) 350 hPa, (b, e) 500 hPa, and (c, f) 850 hPa. The correlation coefficient (*R*), linear fitting coefficient, and RMSE of the fitting residual for COSMIC water vapor retrieval versus ERA5 and ERA-Interim comparisons are listed in each panel.

200

The comparisons between COSMIC and ERA5 water vapor (Fig. 1) suggest overall consistencies over the two selected months and at three pressure levels, which requires further quantitative analysis of the variabilities. In the following sections, we analyze the collocated COSMIC and ERA5 water vapor at three pressure levels to study their spatial (Section 3) and trend (Sections 4 and 5) variabilities (the seasonal trend is provided in Appendix 1).

3. Comparison of Spatial Variability of Water Vapor between COSMIC and ERA5

3.1 Global distribution of COSMIC and ERA5 water vapor

To inter-compare the spatial variability of the water vapor data between COSMIC and ERA5 (interpolated onto COSMIC locations and times), the collocated global humidity data over 12 years (2007-2018) are grouped into 10°x10° latitude/longitude grids and spatial/time-averaged at three selected pressure levels, e.g., 300, 500, and 850 hPa.

Figure 2 compares time-averaged global water vapor distribution maps over three pressure levels between COSMIC (left column) and ERA5 (right column). The overall global distribution of water vapor of COSMIC and ERA5 at three pressure levels is generally consistent. At all three pressure levels, the global water vapor distribution exhibits high concentration in the low latitude tropical regions, decreases rapidly toward the polar region, and is low in some high terrain regions such as the Tibetan Plateau. In the low latitude tropical region, i.e., latitudes between -20 and 20 degrees, increased water vapor concentrations occur in the East Indian and West Pacific Ocean regions and over the Amazon rainforest regions in South America at these three pressure levels. It is noted that COSMIC bending angles are assimilated into ERA5, which especially improves the upper-troposphere and lower-stratosphere temperatures (Hersbach et al. 2020). However, the COSMIC 1DVAR retrieval has more independence from its *a priori* (ERA-Interim) for water vapor within the lower/middle troposphere. Primary water vapor information is retrieved from the RO observations at these altitudes, which our study is focused on. The evaluations of global and latitude-dependent water vapor differences between COSMIC and ERA5 in the following sections would help understand the extent and regional dependence of the assimilation of COSMIC RO water vapor data in ERA5.

To quantitatively evaluate the consistency between COSMIC and ERA5 water vapor (Q) data, the relative biases ($(Q_{COSMIC} - Q_{ERA5})/Q_{ERA5}$ (%)) between COSMIC and ERA5 are calculated with the 12-year collocated COSMIC and ERA5 global water vapor data. The mean differences between COSMIC and ERA5 global water vapor are 5.67±34.30%, -1.86±30.09%, and -2.30±21.21% for pressure levels at 300, 500, and 850 hPa, respectively. This suggests that at 500 and 850 hPa, COSMIC water vapor retrieval is lower than ERA5 water vapor data. This is consistent with the negative moisture biases below 5 km for the RO retrievals compared to the collocated radiosonde data (Ho et al., 2009, 2020a; Shao et al., 2021b). Such near-surface moisture biases may come from the 1DVAR RO retrieval when the super-refraction with a sharp refractivity gradient occurs in the moisture-rich low-troposphere RO profiles (Ho et al., 2020b; Shao et al., 2021a,b). At 300 hPa, the COSMIC water vapor concentration is about 5.67% higher than ERA5. Since the water vapor concentration at 300 hPa is very small, its contribution to the total precipitable water would also be very small. The main cause for higher water vapor retrieved by COSMIC than ERA5 at 300 hPa can be due to the low concentration of water vapor in the upper troposphere and the large uncertainty in retrieving water vapor in the reanalysis model.
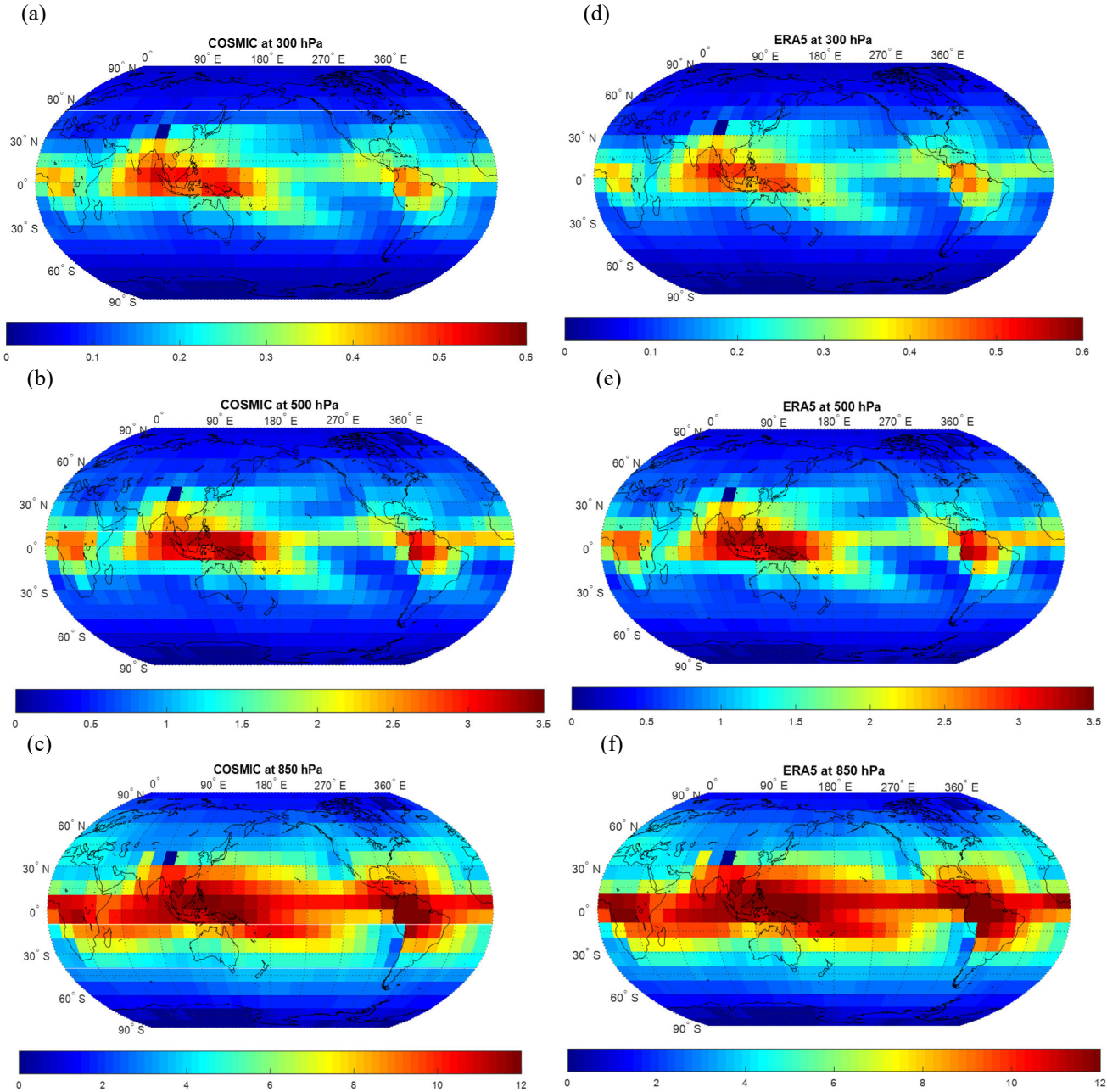
Figure 2: Comparison of the global distribution of 10×10-degree grid-averaged water vapor (g/kg) data between COSMIC retrievals (a, b, c) at 300, 500, 850 hPa, and ERA5 data (d, e, f) at 300, 500, 850 hPa, respectively.

Johnston et al. (2021) analyzed COSMIC-2 and reanalysis models (ERA5 and MERRA2) water vapor differences in different latitude zones. It was shown that the UCAR COSMIC-2 water vapor retrieval in consistently lower than both ERA5 and MERRA2 water vapor data in the lower troposphere (below 2 km). However, COSMIC-2 water vapor retrieval is higher than

250   ERA5 data and lower than MERRA2 data at heights above 4 km. The magnitude of the COSMIC-2 vs. ERA5 water vapor difference is smaller than that of COSMIC-2 vs. MERRA2 above 4 km. The opposite sign and large magnitude of the ERA5 and MERRA2 model water vapor differences relative to COSMIC-2 in the upper troposphere suggest the large uncertainties in retrieving water vapor in the reanalysis model over this height region.

3.2 Latitude-dependence of COSMIC and ERA5 water vapor distribution

255   The comparisons of the latitudinal dependence of water vapor distribution between COSMIC and ERA5 at three pressure levels are shown in Fig. 3. Eight latitudinal bins from -80 to 80 degrees with 20-degree bin width are used to group COSMIC and ERA5 water vapor data. The 20-degree wide latitude bins over northern and southern hemispheres are selected to characterize water vapor latitude-dependence in different reprehensive latitudinal zones such as $0°-20°$ for tropical, $20°-40°$ for sub-tropical, $40°-60°$ for mid-latitude, and $60°-80°$ for high-latitude regions. The regions with latitudes above 80 degrees were

260   not selected due to much less data coverage from COSMIC. The collocated COSMIC and ERA5 water vapor data over all months in 12 years (2007-2018) have been used to calculate the mean water vapor over these latitude bins, as shown in Fig. 3. Figures 3a, 3d, and 3g show the side-by-side comparison of 20-degree latitude-bin-averaged COSMIC and ERA5 water vapor data at 300, 500, and 850 hPa, respectively. The panels in the middle and right columns of Fig. 3 show the latitude-dependence of the COSMIC minus ERA5 water vapor mean difference ($\Delta Q_{COSMIC-ERA5} = Q_{COSMIC} - Q_{ERA5}$) and relative difference

265   $(\Delta Q_{COSMIC-ERA5}(\%) = (Q_{COSMIC} - Q_{ERA5})/ Q_{ERA5} \times 100)$.

In general, both COSMIC and ERA5 water vapor data in Fig. 3 show that latitudinal water vapor distribution peaks in the -20 to 20-degree equatorial latitude zones and rapidly decreases toward the polar region at all three pressure levels. There is an asymmetry in the latitude-dependent distribution of water vapor between the northern and southern hemispheres. For example, the northern hemisphere's 0 to 20-degree equator latitude bin has the highest water vapor compared with all other latitude bins,

270   including the southern -20 to 0-degree latitude bin for all three pressure levels. The decrease of water vapor from the low-latitude tropics to the polar region in the southern hemisphere is more rapid than in the northern hemisphere, which results in a higher water vapor concentration, i.e., wetter, in the north latitudinal bins than those corresponding latitudinal bins in the southern hemisphere.

275   Feulner et al. (2013) showed the asymmetric distribution of annually and zonally averaged surface air temperatures between the northern and southern hemispheres, with the mean surface air temperature in the northern hemisphere being 1–2°C warmer than in the southern hemisphere. Since the warmer temperature is coupled with a higher water vapor evaporation rate, our findings of wetter high-latitude zones in the northern hemisphere are consistent with the interhemispheric temperature difference in Feulner et al. (2013). By analyzing climatological data, the energy budget of Earth, and model simulations,

280   various factors that may cause such interhemispheric temperature differences are compared in Feulner et al. (2013). These factors include seasonal differences in solar radiation, the tropical land area difference, the difference in albedo and temperature

between Antarctic and Arctic polar regions, and particular cross-equatorial ocean heat transport from the colder southern hemisphere to the warmer northern hemisphere. It was shown by Feulner et al. (2013) that for the preindustrial climate, the northward meridional heat transport by ocean circulation, with an additional contribution from the albedo differences between the northern and southern polar regions, are the dominant factors for the interhemispheric temperature difference. With the continued increase of greenhouse gas emissions during the industrial era, the interhemispheric temperature differences grow due to increased land warming than the ocean and the strong loss of Arctic sea ice and snow in the northern hemisphere. These factors affecting interhemispheric temperature difference can affect the interhemispheric water vapor difference.
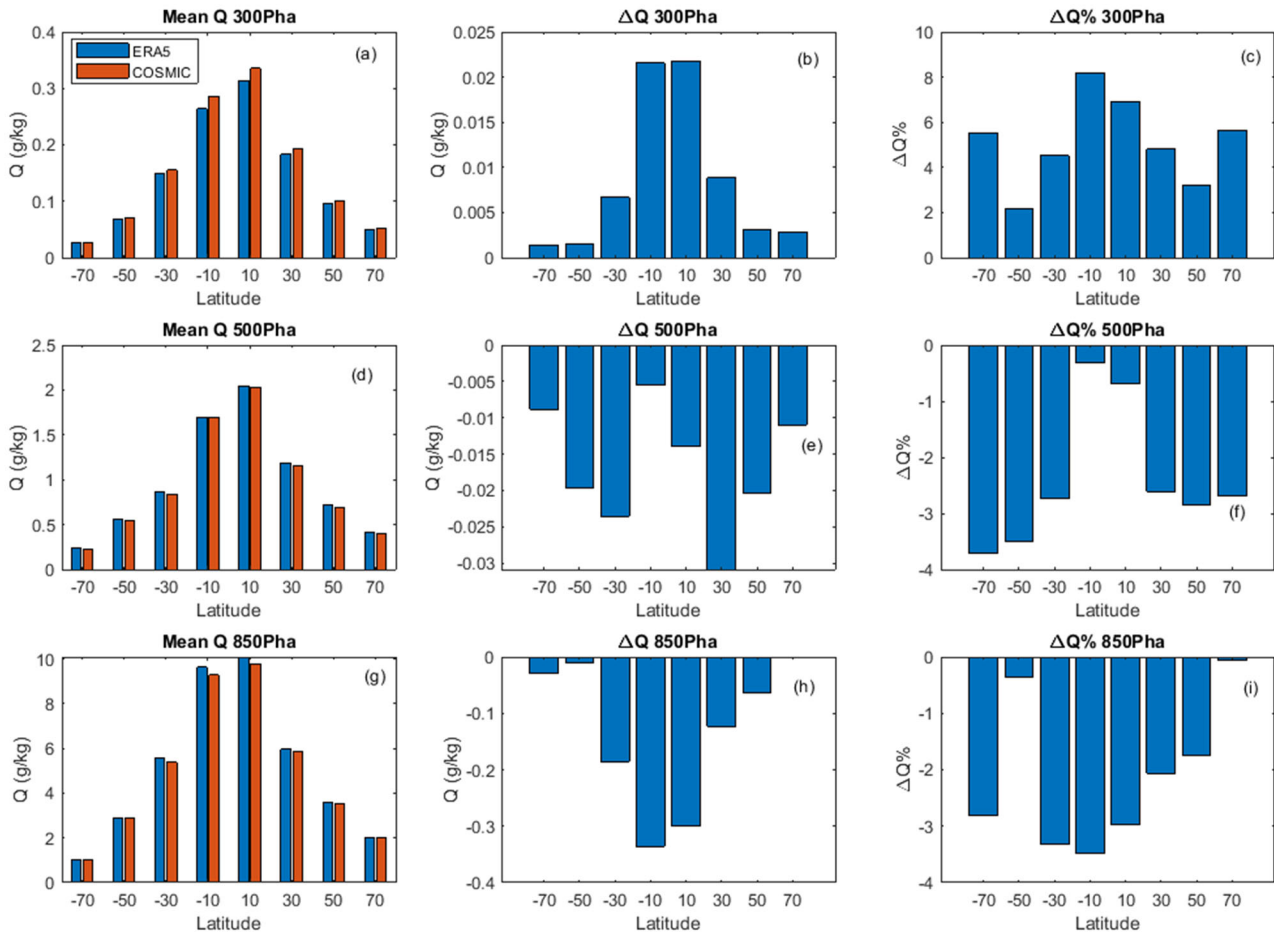
Figure 3: (a, d, g) Comparison of 20-degree latitudinal bin-mean water vapor between COSMIC retrieval and ERA5 data at three pressure levels. Panels (b, e, h) and (c, f, i) show the value-difference and percent-difference (COSMIC minus ERA5) of latitude bin-mean water vapor data between COSMIC retrieval and ERA5 data, respectively. The Top, middle, and bottom rows show the comparisons at 300, 500, and 850 hPa, respectively. In all bar-chart panels, the bar centers on the x-axis are placed at the centers of the 20-degree latitudinal bins. For this figure, collocated COSMIC and ERA5 water vapor data over all months in 12 years (2007-2018) have been used to calculate the mean water vapor in the corresponding latitude bins.

The comparisons between COSMIC and ERA5 water vapor at three pressure levels in the middle and right columns of Fig. 3 show some latitude-dependent differences. At the 300 hPa pressure layer, the mean difference and relative difference $\Delta Q_{COSMIC-ERA5}(\%)$ are all positive (Fig. 3b and 3c), i.e., Q_{COSMIC} being higher than Q_{ERA5}. The peak relative differences (~7-8%) occur in the two equatorial latitude bins (-20 to 0-degree and 0 to 20-degree bins). The percent difference values range from 2% to 8% over the eight latitudinal bins. This suggests that the 5.67% bias in the global Q_{COSMIC} versus Q_{ERA5} comparison mainly comes from the water vapor difference near the equator.

At the 500 hPa pressure level, the $\Delta Q_{COSMIC-ERA5}$ (Fig. 3e) are negative for all the latitude bins, with the amplitude of the water vapor difference being low in the equatorial latitude bins, which is different from those at 300 hPa (Fig. 3b) and 850 hPa (Fig. 3h). At this pressure layer, the mean Q_{COSMIC} is entirely consistent with the mean Q_{ERA5}, i.e., $\Delta Q_{COSMIC-ERA5}(\%)$ is within -0.5% as shown in Fig. 3f, in the -20 to 20-degree latitude bins around the equator. Away from the equator, the percent difference $\Delta Q_{COSMIC-ERA5}(\%)$ increases to around -3%.

At the 850 hPa near-surface level, Fig. 3h and 3j show latitudinal variability with systematic negative biases in $\Delta Q_{COSMIC-ERA5}$ over all eight latitude bins of interest. Figure 3h shows that the amplitudes of negative $\Delta Q_{COSMIC-ERA5}$ are dominantly distributed over the -40 to 40-degree latitude zone while peaking at the -20 to 20-degree equator zone, which agrees with the occurrence of negative water vapor bias in the COSMIC 1DVAR retrieval due to super refraction in the near-surface moisture-rich low latitude regions (Ho et al., 2010). Figure 3j shows that $\Delta Q_{COSMIC-ERA5}(\%)$ of all latitude bins have negative differences around -2% to -3% except for two latitude bins (-60 to -40 degree and 60 to 80 degree) which have $\Delta Q_{COSMIC-ERA5}(\%)$ being larger than -0.3%.

4. COSMIC and ERA5 Water Vapor Time Series Analysis and Trend Comparison after Sampling Errors Removed from COSMIC Data

With six satellites, COSMIC occultations generally have uniform spatial and temporal distributions. However, because the daily sample number of COSMIC occultations decreases dramatically after 2010 (see Fig. A.4e in Appendix), we need to remove the COSMIC sampling uncertainty for the trend calculation. A detailed description of the method to remove sampling uncertainty, i.e., sampling error removal, and calculating trends from water vapor time series data, can be found in Appendix 2 and is not further described here. The COSMIC sampling errors removed water vapor data are used in the rest of the paper. This section focuses on comparing the water vapor trends derived from the COSMIC and ERA5 time series data after sampling error removal and deseasonalized. This section compares the global and latitude-dependent water vapor trends at three pressure levels between COSMIC and ERA5 data. Twelve-year water vapor trends at 300, 500, and 850 hPa from the collocated COSMIC and ERA5 data from 2007 to 2018 are calculated and compared.

4.1 Comparison of global COSMIC and ERA5 water vapor trends

Figure 4a shows the time series of global mean COSMIC and ERA5 water vapor at three pressure levels. At 300 hPa, COSMIC water vapor data is consistently higher than ERA5 data. At 500 and 850 hPa, the COSMIC water vapor data is slightly lower than the ERA5 data. These differences between COSMIC and ERA5 are consistent with the bias analysis in Section 3.1. Figure 4a shows that although the COSMIC and EAR5 time series are different, their trends are pretty close (Figure 4b), which will be further quantified after the time series data are deseasonalized.

It is noted in Fig. 4a that there were two abnormal water vapor increases around 2010 and 2015-2016 in both the COSMIC and ERA5 time series at all three pressure levels. The abnormal increases in water vapor around 2010 and in 2015-2016 were also observed in the long-term total precipitable water monitoring (Mears et al., 2022), which used multiple-RO sensors and radiosonde data to construct the time series data. These abnormal water vapor increases were attributed to El Niño, i.e., the warm phase of the El Niño Southern Oscillation (ENSO). These warm events can enhance surface evaporation, increase tropospheric water vapor, and warm the entire tropical troposphere (e.g., Zveryaev and Allan 2005; Trenberth et al. 2005). The recent 2015-2016 El Niño event broke warming records (according to NINO3.4 and NINO4 indices) in the central Pacific and was among the most significant events recorded in this century. During April 2015 to May 2016 El Niño event, the equatorial Pacific Ocean waters stayed warm for a whole year, reaching peak temperatures in November 2015 (https://www.ecmwf.int/en/newsletter/151/meteorology/2015-2016-el-nino-and-beyond). The long period of warm Pacific Ocean temperature significantly impacted the global weather patterns and diminished seasonal cycles. This also caused the 2015-2016 global atmospheric water concentration anomalies in seasonal variation, as seen in Fig. 4a, through the coupling between ocean and atmosphere over the equatorial Pacific Ocean and the atmospheric winds.

To quantitatively evaluate the trend of global water vapor, Figure 4b shows the time series of sampling error-removed and deseasonalized monthly-mean global water vapor of COSMIC and ERA5 at three pressure levels. The slope values, i.e., long-term trends, are derived with linear regression and listed in Table 1 in both units of g/kg/decade (D_Q) and %/decade (ND_Q). In calculating the percent/decade trend, $i.e.$, normalized trend (ND_Q), the long-term averaged global mean water vapor (g/kg) at a given pressure level has been used to normalize the trend with the unit g/kg/decade.
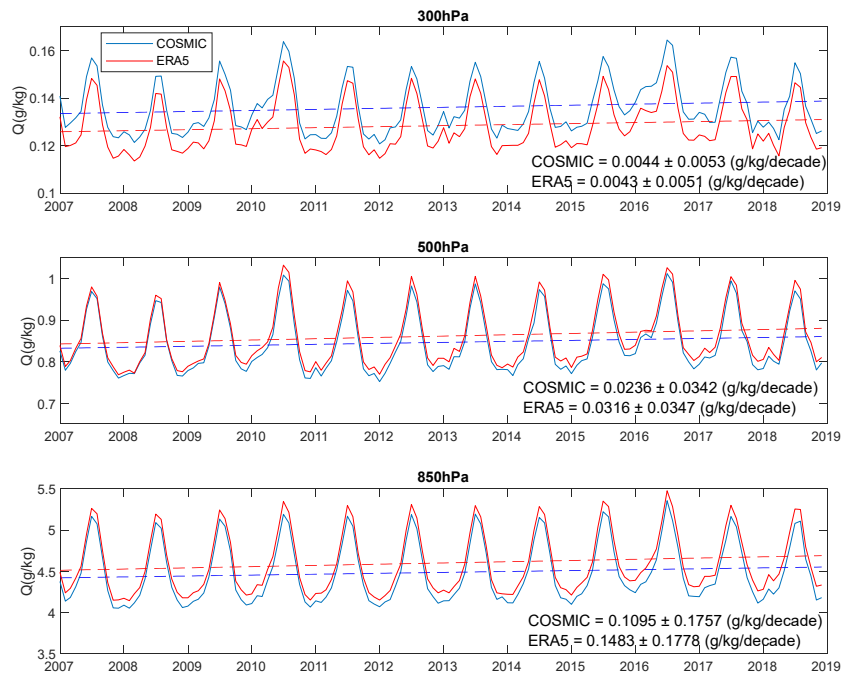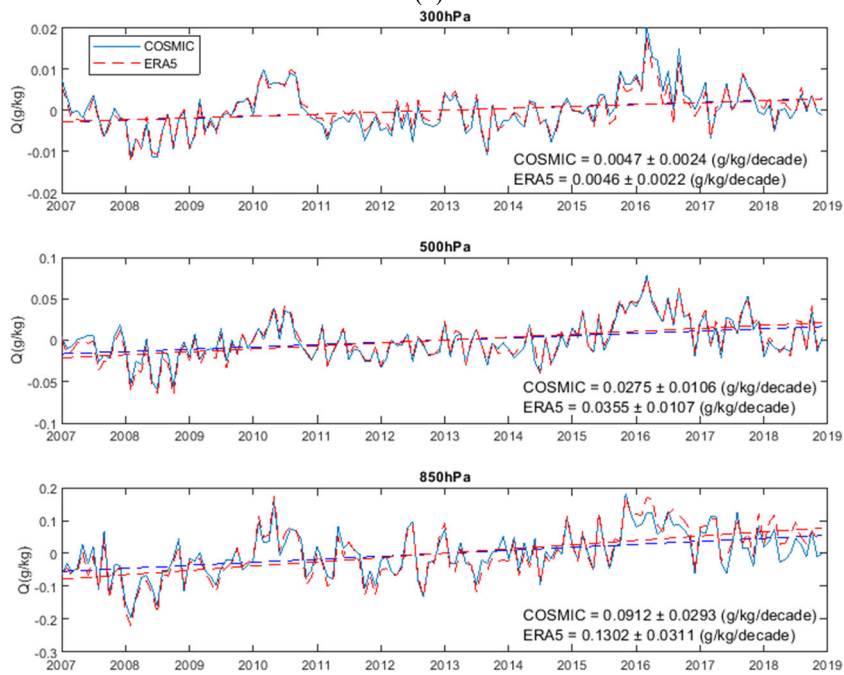
Figure 4: Long-term trending of the global mean of COSMIC and ERA5 water vapor data at three pressure levels. (a) Monthly-mean time series of COSMIC and ERA5 global mean water vapor data at three pressure levels (solid lines) and linear trending lines (dashed lines). (b) Time series of sampling error-removed and deseasonalized monthly-mean COSMIC and ERA5 global water vapor data (solid lines) and linear trending lines (dashed lines). In all panels, red and blue lines are time series (solid lines) and trends (dashed lines) of ERA5 and COSMIC water vapor data, respectively.

COSMIC and ERA5 water vapor trending data in Fig. 4 show that the global water vapor trends at three pressure levels are all positive, suggesting the increase of global water vapor concentration, i.e., becoming globally wetter, over time at these pressure levels. Many earlier studies have reported a rise of global atmospheric water vapor in different periods, e.g., over the period 1979-2001 with ERA-40 reanalysis of ECMWF data in Bengtsson (2004), over the period 1976-2004 with global meteorological data measured by weather stations and marine ships in Dai (2006), and over 1996-2002 with Global Ozone Monitoring Experiment (GOME) data in Wagner et al. (2006). In Chen and Liu (2016), five global PWV data sets, e.g., ECMWF and NCEP reanalysis data, radiosonde, ground GPS stations, and microwave satellite measurements, over the period 2000-2014, were trended, and all show positive global PWV trend. Allan et al. (2022) studied the global-scale changes in water vapor and responses to surface temperature variability since 1979 using coupled and atmosphere-only CMIP6 climate model simulations. In the water vapor trend estimation over the 1988 to 2014 period, Allan et al. (2022) showed a positive increase of global water vapor at the near-surface, at 400 hPa and Column Integrated Water Vapor from an ensemble of climate model simulations with the CMIP6 historical and Atmospheric Model Intercomparison Project (AMIP) experiments. The period of COSMIC RO data studied in this paper partially (2007 to 2014) overlaps with the simulations of Allan et al. (2022). The increasing trend in the global atmospheric water vapor concentration at three pressure levels from our trend analysis is generally consistent with the results from Allan et al. (2022). It was suggested that an increasing trend in water vapor could be the response to the surface temperature increase (Held and Soden, 2006; Santer et al., 2006; Zhang et al., 2013).

Table 1 shows that the increasing trends of global water vapor vary from ~2 to ~4 %/Decade from the analysis of both COSMIC and ERA5 data at three pressure levels. It was also shown by Allan et al. (2022) that in the ensembled historical experimental model simulations, the water vapor increases by 1.53 and 3.52 %/Decade at the surface and at 400 hPa, respectively. Our study shows that the increasing global water vapor trends estimated with 2007-2018 COSMIC data are 2.03±0.65, 3.25±1.25, 3.47±1.47 %/Decade at 850, 500, and 300 hPa, respectively, which are in general agreement with the results from in Allan et al. (2022), considering that the two work cover two distinct periods with 8 overlapped years. In Allan et al. (2022), there is an increase in water vapor trend from the surface to 400 hPa by ~2 %/Decade. Our work shows an increase of positive water vapor trend by 1.44 %/ Decade when height varies from the near-surface (at 850 hPa) to 300 hPa, which is also in general consistent.

Table 1: Comparison of the trending results (slope ± 95% Confidence Interval) between global water vapor trends derived from COSMIC and ERA5 data.

Pressure Level	COSMIC Q Trend ($D_{Q,COSMIC}$, g/kg/Decade)	Normalized COSMIC Q Trend ($ND_{Q,COSMIC}$, %/Decade)	ERA5 Q Trend ($D_{Q,ERA5}$, g/kg/Decade)	Normalized ERA5 Q Trend ($ND_{Q,ERA5}$, %/Decade)
300 hPa	0.0047 ± 0.0024	3.47±1.77	0.0046 ± 0.0022	3.58±1.71
500 hPa	0.0275 ± 0.0106	3.25±1.25	0.0355 ± 0.0107	4.12±1.24

| | 850 hPa | 0.0912 ± 0.0293 | 2.03±0.65 | 0.1302 ± 0.0311 | 2.83±0.68 |

The increasing trend values at 300 hPa derived from COSMIC and ERA5 global water vapor data are consistent. At 500 hPa and 850 hPa, the $ND_{Q,ERA5}$ are higher than COSMIC trends by 0.87%/Decade and 0.8%/Decade, respectively, which suggests that ERA5 may over-estimate the increase of water vapor during 2007 to 2018. Chen and Liu (2016) showed that the increasing PWV trend from 2000 to 2014 derived from ECMWF data is ~0.37%/Decade larger than the PWV trend derived from the ground GPS station data. The difference between $ND_{Q,ERA5}$ and $ND_{Q,COSMIC}$ from our analysis at 500 hPa and 850 hPa are about 0.5%/Decade higher than the differences between the trends of ECMWF and ground GPS station PWV data studied by Chen and Liu (2016).

Using the trending results from COSMIC data, we can also see that water vapor trends increase with lower pressure levels. Table 1 shows that the increasing trend at 850 hPa from COSMIC data ($ND_{Q,COSMIC}$) is lower than at 300 and 500 hPa by 1.44 and 1.22 %/Decade, respectively.

4.2 Comparison of COSMIC and ERA5 latitudinal water vapor trends

To further understand the latitudinal distribution of the water vapor trends, we calculate the trending slopes for COSMIC ($D_{Q,COSMIC}$) and ERA5 ($D_{Q,ERA5}$) in eight 20º latitudinal bins distributed from -80º to 80º latitude range. The latitudinal bins above 80º in the northern and southern polar regions are excluded from this analysis due to too few COSMIC RO observations. Figure 5 compares water vapor trending slope values between COSMIC and ERA5 over eight latitude bins at three pressure levels. The first column of Fig. 5 shows the water vapor trends (D_Q) of unit g/kg/Decade. To account for the latitudinal variation of water vapor, the middle column of Fig. 5 shows the water vapor trends (ND_Q) normalized by the corresponding long-term latitude-bin-averaged water vapor mean and expressed with the unit of %/Decade. The third column of Fig. 5 shows the latitude-dependent water vapor trend difference ($ND_{Q,COSMIC}$ - $ND_{Q,ERA5}$, %/Decade) between COSMIC and ERA5. Table 2 lists the water vapor trend values of COSMIC and ERA5 in eight latitude bins and at three pressure levels.

From Fig. 5, the latitude-mean water vapor trends are mostly positive (increasing), and their magnitudes vary with latitude bins substantially at three pressure levels. The only latitude bin with a small negative water vapor trend with large uncertainty is in the -80º to -60º southern high latitude bin at 500 hPa. From the global surface temperature trend analysis by Gu and Adler, 2022, there is a mixture of a weak decreasing trend in the surface temperature in the Southern Ocean around the Antarctic and an increasing trend over the Antarctic in the -80° to -60° southern latitude bin. However, the uncertainties of estimating both the temperature and water vapor trends in this latitude zone are large.

425 At 300 hPa, the differences in water vapor trends (Fig. 5c) between COSMIC ($ND_{Q,COSMIC}$) and ERA5 ($ND_{Q,ERA5}$) are mixed with positive and negative values and with magnitudes being less than 0.8 %/Decade over the eight latitude bins. In other words, the COSMIC and ERA5 water vapor trends are consistent within 0.8 %/Decade over all eight latitude bins. In Fig. 5b, the trends of water vapor change in the four latitude bins over the -60º to -20º and 20º to 60º zones are in the range of 4 to ~6 %/Decade, which are higher than the water vapor trends (1.79 to 2.58 %/Decade) of the two equatorial latitude bins (0º to 20º

430 and -20º to 0º). The southern -80º to -60º latitude bin has the lowest water vapor trends (both $|ND_{Q,ERA5}|$ and $|ND_{Q,COSMIC}|$ < 0.6%/Decade) at 300 hPa among the eight latitude bins studied in this paper.
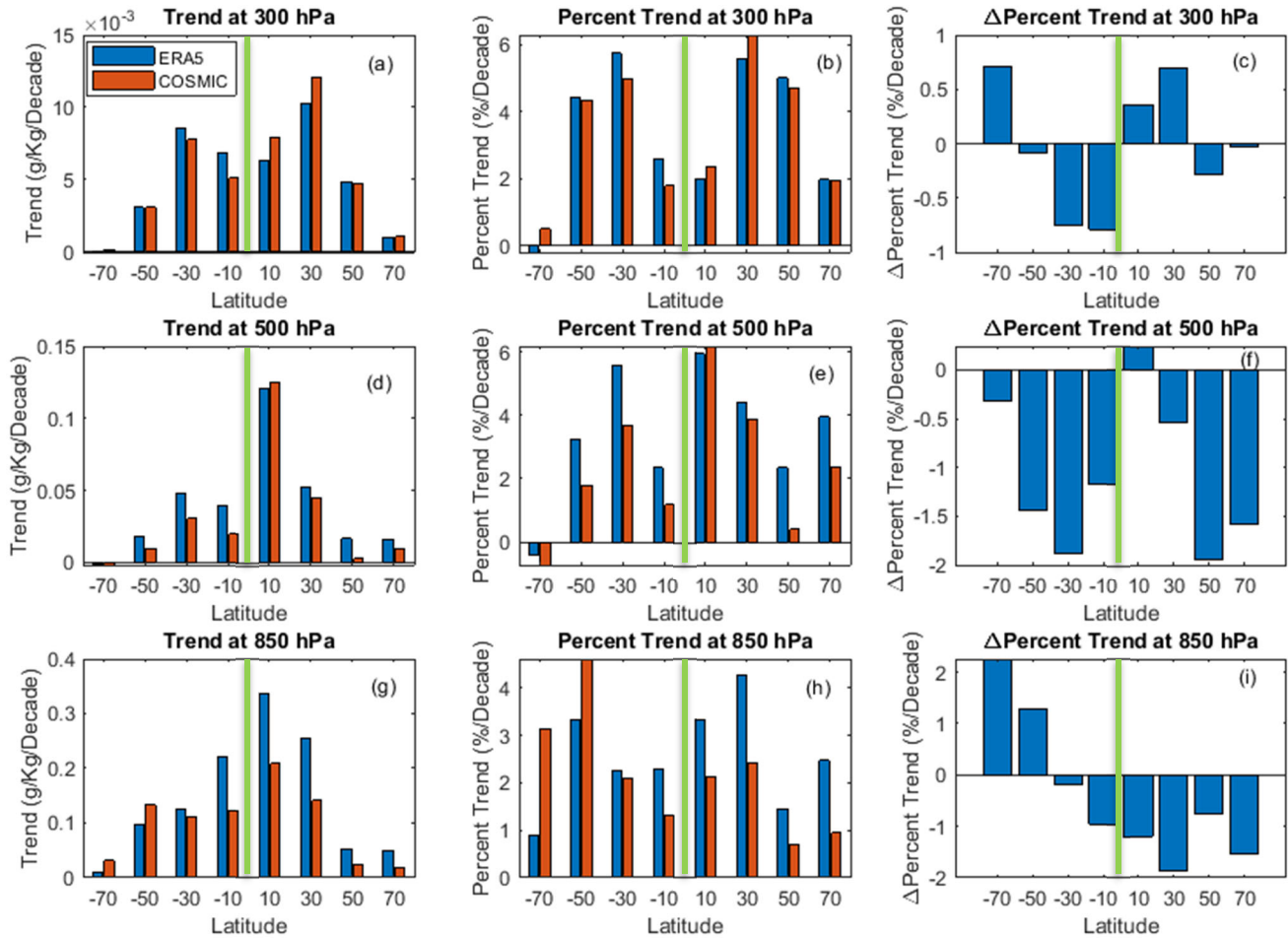
Figure 5: (a, d, g) Comparing the latitude bin-mean water vapor trends (g/kg/Decade) between COSMIC and ERA5 data at 300,
435 **500, and 850 hPa, respectively. (b, e, h) Comparing normalized latitude bin-mean water vapor trends (%/Decade) between COSMIC and ERA5 data at 300, 500, and 850 hPa, respectively. (c, f, i) The difference (COSMIC minus ERA5) of normalized latitude bin-mean water vapor trend (%/Decade) between COSMIC retrieval and ERA5 data at 300, 500, and 850 hPa, respectively. The bar**

centers on the horizontal axis are located at the centers of the 20° latitude bins. The green line in each panel separates the southern (to its left) and northern (to its right) hemispheres.

440

Table 2: Latitude bin-mean water vapor trends (g/kg/Decade and %/Decade) and 95% confidence interval estimated from COSMIC and ERA5 data at 300, 500, and 850 hPa

Latitude Bin	At 300 hPa		At 500 hPa		At 850 hPa	
	$(D_{Q,COSMIC},$ $D_{Q,ERA5})$ (g/kg/Decade)	$(ND_{Q,COSMIC},$ $ND_{Q,ERA5})$ (%/Decade)	$(D_{Q,COSMIC},$ $D_{Q,ERA5})$ (g/kg/Decade)	$(ND_{Q,COSMIC},$ $ND_{Q,ERA5})$ (%/Decade)	$(D_{Q,COSMIC},$ $D_{Q,ERA5})$ (g/kg/Decade)	$(ND_{Q,COSMIC},$ $ND_{Q,ERA5})$ (%/Decade)
-80° to -60°	0.0001±0.0016, -0.00005±0.0016	0.52±5.96, -0.19±6.13	-0.00±0.01, -0.00±0.01	-0.72±6.48, -0.41±6.14	0.03±0.04, 0.01±0.04	3.14±3.87, 0.88±3.61
-60° to -40°	0.0031±0.0039, 0.0031±0.004	4.34±5.58, 4.43±5.72	0.01±0.02, 0.02±0.02	1.80±3.74, 3.25±3.66	0.13±0.06, 0.10±0.06	4.61±2.00, 3.34±1.94
-40° to -20°	0.008±0.0065, 0.0085±0.0064	4.98±4.16, 5.74±4.30	0.03±0.03, 0.05±0.03	3.67±3.85, 5.55±3.74	0.11±0.08, 0.13±0.08	2.09±1.50, 2.27±1.41
-20° to -0°	0.0051±0.0098, 0.0068±0.0091	1.79±3.42, 2.58±3.44	0.02±0.06, 0.04±0.06	1.17±3.52, 2.35±3.50	0.12±0.12, 0.22±0.13	1.33±1.31, 2.29±1.32
0° to 20°	0.0079±0.01, 0.0063±0.0094	2.36±3.04, 2.00±2.98	0.13±0.05, 0.12±0.06	6.17±2.71, 5.93±2.71	0.21±0.10, 0.34±0.10	2.14±1.06, 3.34±1.02
20° to 40°	0.012±0.007, 0.01±0.007	6.29±3.56, 5.59±3.61	0.04±0.03, 0.05±0.03	3.88±2.95, 4.41±2.80	0.14±0.09, 0.25±0.09	2.41±1.61, 4.27±1.56
40° to 60°	0.0047±0.0044, 0.0048±0.0044	4.72±4.40, 5.01±4.48	0.00±0.02, 0.02±0.02	0.40±3.14, 2.35±3.17	0.02±0.08, 0.05±0.08	0.69±2.23, 1.46±2.27
60° to 80°	0.001±0.0031, 0.001±0.003	1.94±5.99, 1.98±6.32	0.01±0.02, 0.02±0.02	2.37±5.38, 3.95±5.25	0.02±0.07, 0.05±0.07	0.94±3.49, 2.48±3.44

445 At 500 hPa, both $D_{Q,COSMIC}$ and $D_{Q,ERA5}$ are the highest (~0.13 g/kg/Decade) in the northern tropical 0° to 20° latitude bin (Fig. 5d). Regarding the normalized trends of the unit %/Decade, the $ND_{Q,COSMIC}$ and $ND_{Q,ERA5}$ (%/Decade) are all positive except in the southern -80° to -60° latitude bin. Over the latitude bins in the -60° to 80° latitude zone, the values of $ND_{Q,ERA5}$ vary between 2.35 and 5.93 %/Decade while values of $ND_{Q,COSMIC}$ vary between 0.4 and 6.17 %/Decade. The water vapor trends of $ND_{Q,COSMIC}$ and $ND_{Q,ERA5}$ in the southern -80° to -60° latitude bin are both quite stable with a weak negative trend within -

450 0.72 %/Decade. Figure 5f shows the difference between $ND_{Q,COSMIC}$ and $ND_{Q,ERA5}$ are all negative (-2 to -0.3 %/Decade) except for one small positive difference (0.24 %/Decade) at the northern equatorial 0° to 20° latitude bin. The smaller global water vapor trend from COSMIC at 500 hPa compared to the trend from ERA5, as shown in Table 1, mainly comes from the latitude bins with negative $ND_{Q,COSMIC}$ - $ND_{Q,ERA5}$ in Fig. 5f. This analysis indicates that at 500 hPa, both ERA5 and COSMIC water vapor data confirm the increasing trends in the -60° to 80° latitude zone and the trends estimated from COSMIC water

455 vapor data are lower than those from ERA5 in most latitude bins except the 0° to 20° equatorial bin.

At 850 hPa, Figure 5g and Table 2 show that the water vapor trends are all positive from the COSMIC and ERA5 data analysis over eight latitude bins at three pressure levels. Regarding the absolute water vapor trend, i.e., of unit g/kg/Decade, the water vapor growth peaks in the northern 0º to 20º equatorial bin and decreases as the latitude increases toward high latitudes. The overall magnitudes of water vapor trends are larger than 0.1 g/kg/Decade from both ERA5 and COSMIC data estimations for the latitude bins in the -40º to 40º latitude zone. The $D_{Q,ERA5}$ is larger by 0.1 to 0.13 g/kg/Decade than $D_{Q,COSMIC}$ in the -20º to 40º latitude zone. The normalized water vapor trends in Fig. 5h and Table 2 show that both $ND_{Q,COSMIC}$ and $ND_{Q,ERA5}$ have substantial variabilities (between 0.69 to 4.61 %/Decade) with latitude bins. Figure 5i shows that $ND_{Q,COSMIC}$ is lower than $ND_{Q,ERA5}$ over the latitude bins from -40º to 80º and $ND_{Q,COSMIC}$ is larger than $ND_{Q,ERA5}$ over the southern latitude bins from -80º to -40º. The magnitude of the difference ($ND_{Q,COSMIC}$- $ND_{Q,ERA5}$) in the -40º to 40º latitude bin is less than 2 %/Decade. This suggests that the differences between COSMIC and ERA5 trends over the middle and low latitude bins are the major contributors to the lower estimated global water vapor trends from COSMIC data than from ERA5 data at 850 hPa (Table 1).

5. Regional Comparisons of COSMIC and ERA5 Water Vapor Trends

5.1 Global map of the 10º×10º COSMIC and ERA5 water vapor trends

To quantify and compare the global distribution of the regional water vapor trends derived from COSMIC and ERA5 data, we grouped the collocated global water vapor data over 12 years (2007-2018) into 10ºx10º latitude/longitude grids. We followed the procedure of estimating the water vapor trend outlined in Appendix 2 to calculate the trends ($D_{Q,COSMIC}$, $ND_{Q,COSMIC}$, $D_{Q,ERA5}$, $ND_{Q,ERA5}$) for the globally distributed 10º×10º RoIs. When the grid size is limited to 10º×10º, there are missing monthly data for certain RoI due to the limited orbital coverage of COSMIC. Figure 6 shows the percentage of missing monthly data distribution over the 2007 to 2018 interval in the global 10º×10º grids. The grids with no missing monthly data during the period are shown as white blanks. The grids with substantial missing monthly data are distributed mostly over northern and southern polar regions with latitudes above 70 degrees. The regions over the Tibetan Plateau also have significant missing monthly data due to the reduced COSMIC RO retrievals over regions with high altitudes. Our 10º×10º RoI-based trending analysis excludes the grids with more than 1.5% missing monthly data at 850 hPa. In other words, grids with > 2-month missing monthly data are excluded from the trend calculation. The effects of sampling error removal on the uncertainty of regional water vapor trend analysis are discussed in Appendix 3.

Figure 7 shows the global distribution of COSMIC and ERA5 water vapor trends ($D_{Q,COSMIC}$ and $D_{Q,ERA5}$) and their difference ($D_{Q,COSMIC} - D_{Q,ERA5}$) at 500 and 850 hPa. The distributions of COSMIC and ERA5 water vapor trends at 300 hPa have smaller regional variations. They are not shown in Fig. 7. In Section 4, Figure 4 and Figure 5 suggest that the global water vapor trends are increasing. The latitude-bin-based water vapor trends are increasing in low and middle latitudes at all three pressure

levels we studied. Figure 7 shows that both COSMIC and ERA5 data indicate substantial regional variabilities in the global distribution of the water vapor trends. The magnitude of water vapor trends peaks near the equator and decreases as it approaches the polar regions, where the atmosphere becomes drier.

490
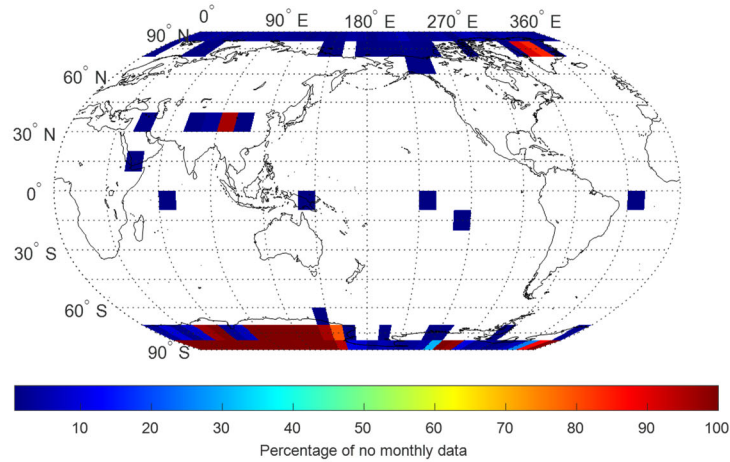
Figure 6: The percentage of missing monthly data over the 2007 to 2018 interval on the global 10º×10º grids. The percentage is shown as color-coded. The grids with no monthly data missing are shown as white blanks.

495   Near the equator, at 500 hPa and 850 hPa, both $D_{Q,COSMIC}$ and $D_{Q,ERA5}$ are strongly positive, i.e., becoming wetter over time, around 180º to 240º longitude and 10º to 20º latitude range in the equatorial Pacific Ocean. This region in the Pacific Ocean with a strong positive water vapor trending slope is encased at the west side by two regions with negative water vapor trends located around (Latitude: 20º; Longitude: 130º) and (Latitude: -10º; Longitude: 130º) which are on the northern and southern side, respectively. These two regions are located in the western Pacific and the eastern Indian Ocean interface, where sizeable

500   regional moisture flux convergence occurs (Fig. 2). Such a pattern of strong increasing water vapor slope in the equatorial Pacific Ocean and decreasing water vapor slope near the interface between the west Pacific and the east Indian Ocean are more prominent at 500 hPa than at 850 hPa. At 500 hPa, the negative water vapor slopes are extended to northern Australia and southern Asia, covering the Indo-Pacific warm pool region. Sea surface temperature has been increasing in the western Pacific during recent decades (e.g., Gu and Adler 2022). There is a high correspondence with regard to the trends in sea surface

505   temperature and tropospheric water vapor in the western Pacific during the recent decades (e.g., Gu and Adler 2013). It was shown by Chen and Liu (2016) that the moderate increase in surface temperature over the Pacific Ocean could cause the PWV to increase in the equatorial region of the Pacific Ocean and decrease in this Indo-Pacific warm pool region, which is what we observe here. Further quantitative analysis of trends at selected locations in the Pacific Ocean (Sites # 4, 16 in Fig. 8) and in the Indo-Pacific warm pool region (Site #14 in Fig. 8) will be performed in the following sections.
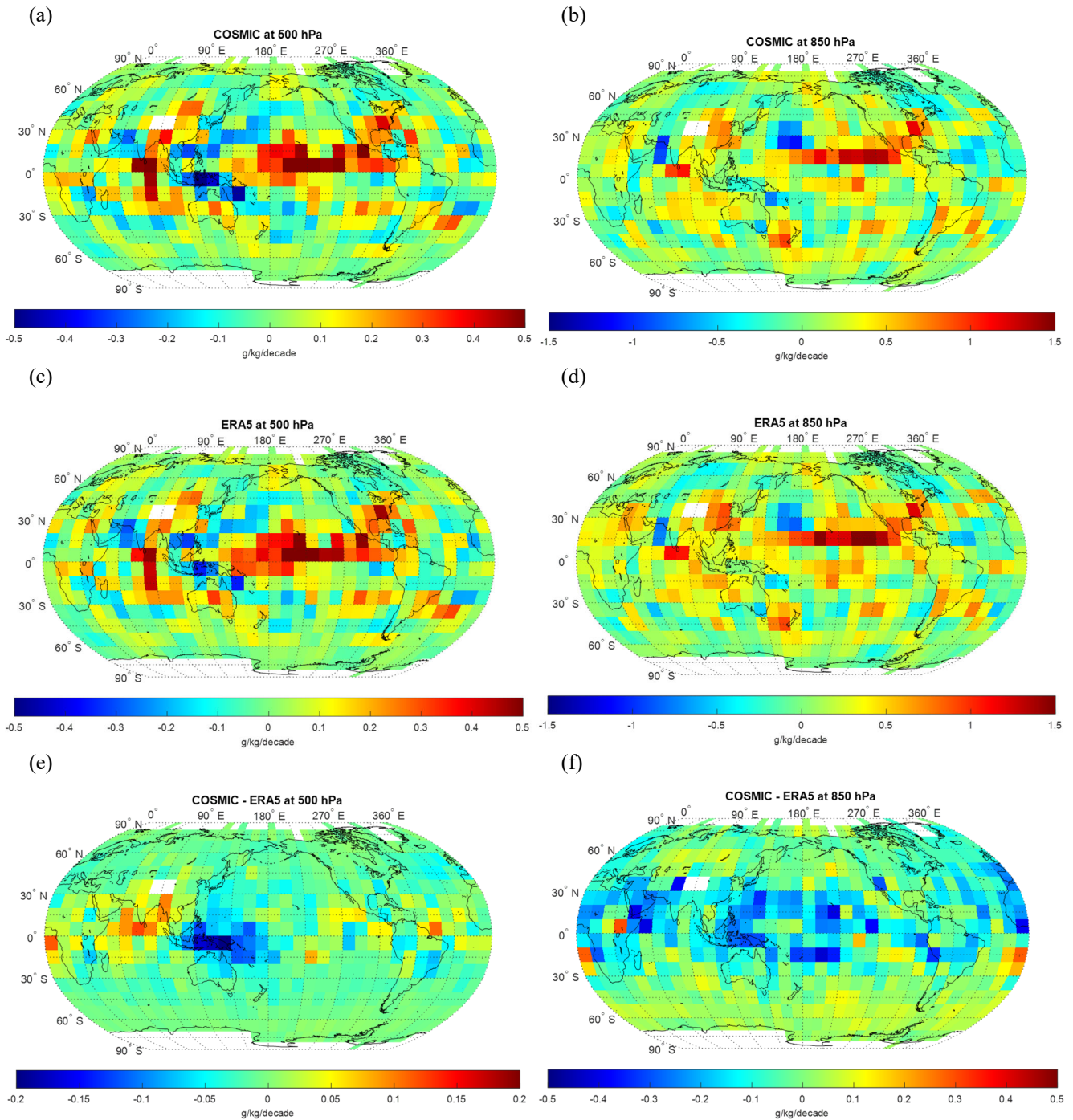
510

Figure 7: (a, b) and (c, d) The global distribution of water vapor trending slope (g/kg/Decade) in $10^o \times 10^o$ grids derived from long-term COSMIC (a, b) and ERA5 (c, d) data, respectively; (e, f) The global distribution of the water vapor trending slope difference (g/kg/decade) between COSMIC and ERA5 (COSMIC minus ERA5). The left and right columns are derived with water vapor data at 500 and 850 hPa, respectively.

525 In the Indian Ocean, the region (Latitude: 0º to 10º; Longitude: 70º to 90º) in the Laccadive Sea near the northern edge of the Indian Ocean has strong increasing water vapor trends at 850 hPa. At 500 hPa, the region with strong positive water vapor trends expands to a larger region (Latitude: -20º to 10º; Longitude: 80º to 90º). This region is affected by the monsoon climate over the south of the Himalayas, resulting in a sizeable regional change in precipitation at different seasons. Indian Ocean is an essential part of the coupled Indian monsoon system because it feeds the moist convection over both land and ocean.

530 Convection, precipitation, and water vapor are also fully coupled processes. It is shown that the Indian Ocean has been warming up during the recent decades (Gu and Adler, 2022), which is the driver for the positive water vapor trend in this region. The region (Latitude: 10º to 30º; Longitude: 60º to 70º) near the Gulf of Oman in the Arabian Sea has strong decreasing water vapor trends at 850 hPa. At 500 hPa, this region with negative water vapor trends expands to the area with Latitude: 10º to 30º; Longitude: 50º to 80º and covers the northern coast.

535

Over the land, a significantly increasing water vapor trend at 850 hPa can be observed around the region (Latitude: 30º to 40º; Longitude: 270º to 280º) in the eastern United States and over the region (Latitude: 20º to 40º; Longitude: 110º to 130º) near southern and eastern China.

540 In the following sections, we selected a few representative sites, such as stratocumulus cloud-rich sites (section 5.2), sites with notable increasing (wetter) and decreasing (drier) water vapor trends (Section 5.3), and sites with a notable difference between ERA5 and COSMIC trends (Section 5.4) to understand the spatial variability of water vapor trends. Their center locations are shown in Fig. 8. These established sites are in 10º by 10º latitude/longitude grids.
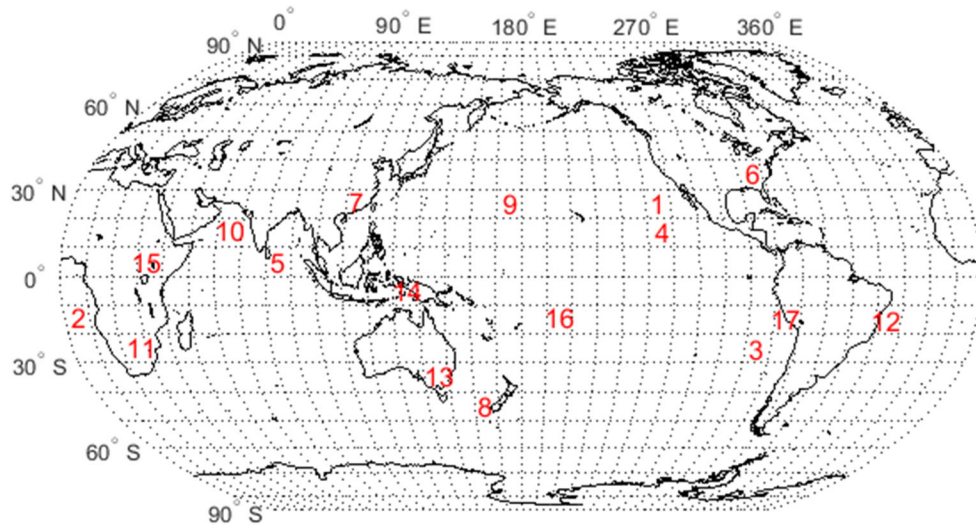
545

Figure 8: Center locations of selected sites for regional analysis of water vapor trends.

5.2 Water vapor trends over stratocumulus cloud-rich regions

The first set of sites we selected is over stratocumulus cloud-rich regions. Stratocumulus clouds are typically shallow and occur at low heights (below 2 km) due to being driven by weak convective currents with drier and stable air above, preventing continued vertical development. Stratocumulus clouds usually occur over subtropical and polar oceans. Over regions with frequent stratocumulus clouds, it is challenging to accurately estimate water vapor at low heights in the ECMWF assimilation (Lonitz and Geer 2017). On the other hand, the RO signal can penetrate the cloud because the wavelengths for L1 and L2 frequency of RO signals are around 19 cm and 24.2 cm, respectively, which are much larger than the size of cloud water droplets and ice crystals (Kursinski et al., 1997). The water vapor retrieval from RO data is not affected by the cloud. Therefore, we will compare the near-surface water vapor trend of ERA5 and COSMIC at 850 hPa over three stratocumulus cloud-rich regions. Table 3 lists the water vapor trends at 500 and 850 hPa over three sites in the ocean: West of the Baja coast (#1), West of Africa (#2), and West of South America (#3), derived from COSMIC and ERA5 data. These three regions are selected according to the stratocumulus cloud-rich regions identified by Wood et al., 2011, Wood, 2012 and Ho et al., 2015.

Table 3: Water vapor trends over three selected stratocumulus cloud-rich sites.

	Center (Lat., Long.) Region	At 500 hPa			At 850 hPa		
		$(\overline{Q_{COSMIC}}, \overline{Q_{ERA5}})$ (g/Kg)	$(D_{Q,COSMIC}, D_{Q,ERA5})$ (g/kg/Decade)	$(ND_{Q,COSMIC}, ND_{Q,ERA5})$ (%/Decade)	$(\overline{Q_{COSMIC}}, \overline{Q_{ERA5}})$ (g/Kg)	$(D_{Q,COSMIC}, D_{Q,ERA5})$ (g/kg/Decade)	$(ND_{Q,COSMIC}, ND_{Q,ERA5})$ (%/Decade)
Site #1	(25°, 235°) West of Baja coast	0.77±0.28, 0.82±0.52	0.12±0.24, 0.10±0.24	15.19±30.63, 12.37±28.79	4.12±1.42, 3.83±2.26	0.61±0.84, 0.53±0.85	14.76±20.34, 13.92±22.10
Site #2	(-15°, 5°) West of Africa	0.83±0.49, 0.84±0.74	0.09±0.28, 0.03±0.27	10.97±33.23, 3.94±32.44	4.38±1.55, 4.74±2.13	0.36±0.72, 0.07±0.71	8.13±16.49, 1.51±14.94
Site #3	(-25°, 275°) West of South America	0.49±0.15, 0.52±0.32	0.21±0.15, 0.22±0.15	42.66±29.67, 42.64±28.13	3.91±1.10, 3.91±1.60	0.16±0.63, 0.06±0.64	4.02±16.06, 1.56±16.24

At 850 hPa, COSMIC and ERA5 data show these three sites have comparable mean water vapor (around 4 g/kg). At 500 hPa, site #3 has a lower mean water vapor than the other two sites. These three sites have increasing water vapor trends at 500 and 850 hPa. At 850 hPa, Site #1 has the strongest increasing trend of water vapor and $ND_{Q,COSMIC}$ (14.76 %/Decade) is comparable to $ND_{Q,ERA5}$ (13.92 %/Decade). For Site #2 and #3, there are significant differences between the trends estimated with COSMIC and ERA5 data at 850 hPa. For example, the increasing trend estimated from COSMIC ($ND_{Q,COSMIC}$) is about 6.62 %/Decade higher than $ND_{Q,ERA5}$ for Site #2 (Table 3). For Site #3, the $ND_{Q,COSMIC}$ is higher than $ND_{Q,ERA5}$ by 2.46 %/Decade. This analysis indicates that for two of the three selected sites around the stratocumulus cloud-rich regions, the estimated water vapor trends from COSMIC at 850 hPa can be significantly higher than those estimated from ERA5 data. The possible cause of smaller trends from ERA5 water vapor data over stratocumulus cloud-rich regions could be the difficulty in accurately

estimating water vapor at low heights in ERA5 reanalysis data compared with COSMIC RO measurements that are unaffected by stratocumulus cloud (Lonitz and Geer, 2017).

5.3 Sites with notable increasing and decreasing water vapor trends

A few sites were selected with notable increasing and decreasing water trends. To select these sites, we searched the $10^\circ \times 10^\circ$ global grids and identified the regions with the largest increasing and decreasing water vapor trends. Within these regions, we selected the representative sites, and their trend data are listed in Table 4 and Table 5.

In Table 4, both COSMIC and ERA5 trend data show increasing water vapor trends at 500 hPa and 850 hPa for the five selected sites. Site#4, #5, and #8 are in the ocean, and sites #6 and #7 are on the land. The sites #4, #5, and #7 have substantial mean water vapor (> 7.5 g/kg at 850 hPa and > ~1.5 g/kg at 500 hPa). At 850 hPa, the mean water vapor from COSMIC is lower than ERA5 for all five sites in Table 4. The trends between COSMIC and ERA5 are consistent with $|ND_{Q,COSMIC} - ND_{Q,ERA5}| <$ 2.7 %/Decade at 850 hPa for these five sites. Site #6 (latitude: 30° to 40°; longitude: 270° to 280°) over land in the United States has the strongest increasing water vapor trend: > 18%/Decade at 850 hPa and > 39%/Decade at 500 hPa among all of the 10° by 10° grids over land. Sites #4 and #8 have large increasing water vapor trends (> 17 %/Decade and > 23 %/Decade, respectively) among the sites over the ocean. Many previous studies have explored the trends in surface temperature (e.g., Gu and Adler, 2022 and references therein). Global surface keeps warming up, though with rich spatial structures of temperature change. From the study by Gu and Adler, 2022, ocean surface warming can readily be seen in the Indian Ocean and tropical Pacific Ocean, roughly corresponding to the strong increasing tropospheric water vapor trends for Sites #4, #5, and #8 we observed.

Table 5 lists the water vapor trends for five sites with notable decreasing trends. Sites #9 and #10 are over the ocean, and Sites #11, #12, and #13 are over land. For the two ocean sites, water vapor trends at 500 and 850 hPa from COSMIC and ERA5 are strongly negative (mostly < -10 %/Decade). These two ocean sites accompany the regions with strong positive water vapor trends over the equatorial Pacific Ocean and the Laccadive Sea, respectively (Fig. 7). The long-term negative water vapor trend at 850 hPa for Site #11 in southern Africa can cause a regional drier atmosphere. Site #12 in Brazil has a mild decreasing water vapor trend at 850 hPa and a strong decreasing water vapor trend (< -10%/Decade) at 500 hPa from COSMIC data. Site #13 in Australia has the lowest mean water vapor, i.e., dry, among the five sites and a strong decreasing trend (< -10%/Decade at 850 hPa), which can result in a long-term drier atmosphere in this region (Dai et al., 2006; Zhang et al., 2018).

605

Table 4: Water vapor trends over selected sites with notable increasing trends.

	Center (Lat., Long.) Region	At 500 hPa			At 850 hPa		
		$(\overline{Q_{COSMIC}}, \overline{Q_{ERA5}})$ (g/Kg)	$(D_{Q,COSMIC}, D_{Q,ERA5})$ (g/kg/Decade)	$(ND_{Q,COSMIC}, ND_{Q,ERA5})$ (%/Decade)	$(\overline{Q_{COSMIC}}, \overline{Q_{ERA5}})$ (g/Kg)	$(D_{Q,COSMIC}, D_{Q,ERA5})$ (g/kg/Decade)	$(ND_{Q,COSMIC}, ND_{Q,ERA5})$ (%/Decade)
Site #4	(15º, 235º) West of Baja coast	1.48±0.53, 1.53±0.81	0.44±0.34, 0.39±0.34	29.56±22.99, 25.46±22.08	7.68±1.87, 8.49±2.47	1.36±0.79, 1.51±0.78	17.71±10.22, 17.73±9.17
Site #5	(5º, 85º) Laccadive Sea	2.86±0.66, 2.83±1.00	0.58±0.39, 0.48±0.40	20.28±13.79, 16.99±13.97	10.96±1.13, 11.11±1.29	1.08±0.51, 1.06±0.50	9.83±4.67, 9.55±4.51
Site #6	(35 º, 275º) United States	1.04±0.46, 1.10±0.61	0.41±0.24, 0.47±0.23	39.48±22.71, 42.67±21.34	5.93±2.85, 6.61±3.17	1.18±0.82, 1.22±0.81	19.91±13.78, 18.40±12.20
Site #7	(25º, 115º) Southeast China	2.00±1.13, 1.96±1.27	0.13±0.30, 0.11±0.29	6.44±14.80, 5.65±14.99	9.31±3.15, 9.34±3.57	0.70±0.85, 0.86±0.85	7.52±9.18, 9.21±9.08
Site #8	(-45º, 165º) Near New Zealand	0.62±0.20, 0.70±0.33	0.10±0.13, 0.10±0.13	15.60±21.43, 14.13±18.75	3.67±0.64, 3.98±1.34	0.95±0.54, 0.92±0.54	25.77±14.73, 23.10±13.56

Table 5: Water vapor trends over selected sites with notable decreasing trends.

	Center (Lat., Long.) Region	At 500 hPa			At 850 hPa		
		$(\overline{Q_{COSMIC}}, \overline{Q_{ERA5}})$ (g/Kg)	$(D_{Q,COSMIC}, D_{Q,ERA5})$ (g/kg/Decade)	$(ND_{Q,COSMIC}, ND_{Q,ERA5})$ (%/Decade)	$(\overline{Q_{COSMIC}}, \overline{Q_{ERA5}})$ (g/Kg)	$(D_{Q,COSMIC}, D_{Q,ERA5})$ (g/kg/Decade)	$(ND_{Q,COSMIC}, ND_{Q,ERA5})$ (%/Decade)
Site #9	(25 º, 175 º) North Pacific Ocean	1.13±0.46, 1.27±0.73	-0.15±0.29, -0.10±0.29	-13.36±25.53, -7.55±22.76	7.85±1.71, 8.01±1.97	-1.09±0.64, -0.85±0.64	-13.93±8.20, -10.62±7.98
Site #10	(15 º, 65 º) Arabian Sea	1.30±0.92, 1.39±1.17	-0.16±0.36, -0.26±0.36	-12.59±27.49, -18.40±25.95	7.23±2.65, 7.35±3.15	-0.91±0.82, -0.74±0.79	-12.55±11.30, -10.05±10.78
Site #11	(-25 º, 25 º) Ngwaketse, Botswana	1.25±0.86, 1.11±0.95	0.01±0.29, 0.04±0.29	0.59±23.40, 3.92±26.29	6.72±2.67, 6.80±2.95	-0.43±0.70, -0.34±0.72	-6.33±10.40, -5.06±10.62
Site #12	(-15 º, 315 º) Brazil	1.60±0.94, 1.59±1.24	-0.17±0.42, -0.09±0.42	-10.42±26.10, -5.66±26.49	9.88±1.78, 10.28±1.95	-0.29±0.47, -0.12±0.47	-2.96±4.79, -1.13±4.59
Site #13	(-35 º, 145 º) Australia	0.65±0.28, 0.73±0.48	0.17±0.20, 0.18±0.19	25.79±30.55, 23.97±26.53	4.27±1.05, 4.58±1.57	-0.56±0.57, -0.49±0.58	-13.09±13.41, -10.74±12.69

610

5.4 Sites with a notable water vapor trend difference between ERA5 and COSMIC

Figure 7a-d show that the global distribution of water vapor trends is generally consistent between $D_{Q,COSMIC}$ and $D_{Q,ERA5}$ at 500 and 850 hPa. More quantitatively, we show the spatial distribution of the $D_{Q,COSMIC}$ - $D_{Q,ERA5}$. i.e., the water vapor trend differences between COSMIC and ERA5, at 500 and 850 hPa in Fig. 7e and 7f, respectively. At 500 hPa, the negative

615 differences ($D_{Q,COSMIC} < D_{Q,ERA5}$) are primarily distributed in the regional box (latitude: -10 to 10-degree; longitude: 120 to 170-degree) where the Indo-Pacific Ocean region is located, and the decreasing water vapor trends are observed by both COSMIC and ERA5. The difference is positive at 500 hPa, i.e., $D_{Q,COSMIC} > D_{Q,ERA5}$, in the northern Indian Ocean and near its north coast. At 850 hPa, the difference is primarily negative, with the COSMIC trend being lower than ERA5 in tropical

areas. Only in a few regions located around sites #2 and #15, the $D_{Q,COSMIC}$ is higher than $D_{Q,ERA5}$. Such dominantly negative differences between $D_{Q,COSMIC}$ and $D_{Q,ERA5}$ in tropical regions (30°S to 30°N) at 850 hPa determines the lower global and low-latitude $D_{Q,COSMIC}$ in comparison with $D_{Q,ERA5}$ as shown in Table 1, 2 and Fig. 5.

Table 6 lists the water vapor trend data of four sites we selected with notable COSMIC and ERA5 trend differences. Sites #14 and #16 are over the ocean, and sites #15 and #17 are over land. Sites #14, #15, and #16 are all moisture-rich sites. Site #14 is located in the Indo-Pacific Ocean region, which suggests large uncertainty in the characterization of $D_{Q,ERA5}$ in this region. Site #15 is among the very few sites (Fig. 7f) with $D_{Q,COSMIC}$ larger than $D_{Q,ERA5}$ (by 0.29 g/kg/Decade) at 850 hPa. Site #16 is the typical low-latitude site with $D_{Q,COSMIC}$ being less than $D_{Q,ERA5}$. For site #17 in Peru, COSMIC shows a much steeper decreasing trend, lower by -8.34 %/Decade, than ERA5 at 850 hPa. This area is mixed with Andes Mountains on the east and the Pacific Ocean on the west. There are no 850 hPa RO data over the Andes Mountains (over 6 km in height) area. The RO water vapor trend data mostly come from the nearby Pacific Ocean on the west. The COSMIC water vapor trend indicates that Site #17 has decreased near-surface water vapor from 2007 to 2018, while ERA5 data suggests no significant long-term change in the amount of water vapor. From the study of a linear trend in global surface temperature during 1998-2020 by Gu and Adler, 2022, there is a trend of decreasing ocean surface temperature (~-0.1 K/Decade) near Site #17, which matches the decrease of water vapor observed by COSMIC. This site is near Site #3 and is affected by a nearby low-height stratocumulus cloud, which makes it more challenging to accurately estimate water trends from ERA5 data than from COSMIC data.

The dominantly negative trend differences between $D_{Q,COSMIC}$ and $D_{Q,ERA5}$ in low-latitude regions at 850 hPa, and the notable large trend difference between COSMIC and ERA5 over sites #5, #14-#17 are all concentrated within the northern and southern boundaries of the Intertropical Convergence Zone (ITCZ) area. The ITCZ encircles Earth near the thermal equator and is where trade winds converge between the northeast (in the northern hemisphere) and the southeast (in the southern hemisphere). The specific position of ITCZ varies seasonally. The ITCZ has concentrated deep clouds spanning nearly the entire circumference of the equatorial regions, one of the most prominent atmospheric circulation features. Johnston et al. (2021) investigated the distribution and variability of COSMIC-2 water vapor by comparing it to collocated ERA5 and MERRA-2 reanalysis profiles in the tropical and subtropical regions. It was found by Johnston et al. (2021) that the largest moisture differences and weakest correlations were typically observed in regions that experience frequent convection, such as along the ITCZ, over the Indo-Pacific warm pool, or in central Africa. These locations match what we found in our paper. Our explanation for such difference is that for regions with frequent atmospheric circulation, such as deep clouds, the RO retrievals may characterize water vapor distribution and occurrence better than ERA5 due to the cloud-penetrating ability of GPS signal and higher height-resolution in RO data to resolve sharp moisture gradient better.

Table 6: Water vapor trends over selected sites with notable COSMIC and ERA5 trend differences.

	Center (Lat., Long.) Region	At 500 hPa			At 850 hPa		
		$(\overline{Q_{COSMIC}},$ $\overline{Q_{ERA5}})$ (g/Kg)	$(D_{Q,COSMIC},$ $D_{Q,ERA5})$ (g/kg/Decade)	$(ND_{Q,COSMIC},$ $ND_{Q,ERA5})$ (%/Decade)	$(\overline{Q_{COSMIC}},$ $\overline{Q_{ERA5}})$ (g/Kg)	$(D_{Q,COSMIC},$ $D_{Q,ERA5})$ (g/kg/Decade)	$(ND_{Q,COSMIC},$ $ND_{Q,ERA5})$ (%/Decade)
Site #14	(-5°, 135°) Arafura Sea	3.24±0.63, 3.33±0.82	-0.42±0.34, -0.25±0.33	-13.09±10.44, -7.39±9.81	11.44±1.14, 11.88±0.99	-0.27±0.37, 0.03±0.35	-2.40±3.27, 0.26±2.98
Site #15	(5°, 35°) South Sudan	2.41±0.83, 2.29±0.85	0.00±0.30, -0.01±0.29	0.13±12.33, -0.53±12.49	10.24±1.63, 10.71±1.72	0.32±0.45, 0.03±0.42	3.17±4.40, 0.24±3.93
Site #16	(-15°, 195°) South Pacific Ocean	1.98±0.78, 1.97±1.08	-0.02±0.39, -0.01±0.39	-0.77±19.94, -0.58±19.96	10.37±1.19, 10.96±1.27	0.04±0.44, 0.46±0.44	0.35±4.21, 4.18±4.01
Site #17	(-15°, 285°) Peru	1.24±0.55, 1.78±0.75	-0.01±0.28, 0.03±0.27	-1.07±22.55, 1.42±15.13	4.05±2.15, 6.11±1.81	-0.34±0.42, -0.01±0.34	-8.51±10.38, -0.17±5.63

6. Conclusions and Discussions

655 This paper evaluates the spatiotemporal consistency and difference between UCAR COSMIC (WETPrf) and ECMWF's ERA5 global reanalysis of water vapor data from 2007 to 2018. The analysis of temporal variability focuses on the long-term trends and seasonal variability of COSMIC and ERA5 water vapor data. Spatial variabilities of global, latitudinal, and regional distribution of COSMIC and ERA5 mean water vapor and trends at three pressure levels (300, 500, and 850 hPa) are analyzed and quantitatively compared. These two water vapor datasets generally show good agreements in spatiotemporal distributions

660 and trends.

The key comparison results of time-averaged water vapor between COSMIC and ERA5 can be summarized as follows:

i) COSMIC water vapor retrievals are more consistent with ERA5 reanalysis data than ERA-Interim, which suggests that from the data assimilation point of view, COSMIC water vapor is closer to the true state of the atmosphere, i.e.,

665 the impacts from ERA-Interim in the UCAR COSMIC 1DVAR retrieval processing is minimum. It is noted that the coordinated efforts from Stratosphere–troposphere Processes And their Role in Climate (SPARC) Reanalysis Inter-comparison Project (S-RIP) plays an important role in comparing reanalysis datasets using a variety of key diagnostics and particularly confirmed the significant improvements of the latest version of reanalyses in ERA5 compared to ERA-interim (Fujiwara et al., 2017).

670 ii) At 300, 500, and 850 hPa, the differences between COSMIC water vapor retrievals and water vapor from ERA5 over the globe are 5.67±34.30%, -1.86±30.09%, and -2.30±21.21%, respectively. Ho et al. (2010) and Shao et al. (2021b) showed systematic negative water vapor biases below 5 km for RO retrievals in comparison with radiosonde data. Such negative water vapor biases can be traced to the negative RO bending angle biases when compared with the reanalysis model (Ho et al., 2020a). The negative water vapor biases below 5 km, *e.g.*, at 500 and 850 hPa as

675 studied in this paper are mainly due to the underestimation of water vapor in RO retrieval in the presence of

atmospheric super-refraction or ducting in the moisture-rich low-troposphere (Sokolovskiy, 2003; Ao et al., 2003; Xie et al., 2006; Ao, 2007). Super-refraction occurs when the vertical atmospheric refractivity gradient exceeds a critical refraction threshold, *i.e.,* in the presence of a sharp change in refractivity. Such sharp change often exists around the planetary boundary layer, where sharp vertical gradients in moisture and temperature inversion are frequently observed. To address the negative moisture biases in RO retrieval and account for super-refraction or ducting, there are efforts to improve the 1DVAR retrieval algorithm by incorporating the reconstruction method introduced by Xie et al. (2010). Our study shows that the negative water vapor biases at 850 hPa are dominantly in the -40º to 40º (tropical and sub-tropical) moisture-rich regions. This study does show that the global (Fig. 4 and Table 1) water vapor trends are, in general, consistent with ERA5 at 500 and 850 hPa, although the negative water vapor biases are present at these two pressure levels. At 300 hPa, there is a positive bias in COSMIC global water vapor compared to ERA5. Johnston et al. (2021) showed opposite signs of the ERA5 and MERRA2 model water vapor differences relative to COSMIC-2 in the upper troposphere. The positive bias we observed is consistent with Johnston et al. (2021) and can be due to the large uncertainties in retrieving water vapor in the reanalysis model in the upper troposphere with a low concentration of water vapor.

iii)   Latiude-dependence study shows the asymmetry in the latitudinal distribution of water vapor between the northern and southern hemispheres. There was a more rapid decrease of water vapor from the low-latitude tropical to the polar region in the southern hemisphere than in the northern hemisphere. The inter-hemispheric water vapor difference can be traced to the inter-hemispheric difference in temperature (Feulner et al., 2013).

The key findings from the trends estimating from 2007-2018 COSMIC and ERA5 water vapor data at global, latitudinal, and regional (10 by the 10-degree grid) levels are summarized as follows:

i)   The anomalous increase of water vapor around 2015-2016 is identifiable in the COSMIC and ERA5 time series of water vapor data at all three pressure levels and was attributed to an El Niño event from April 2015 to May 2016.

ii)   COSMIC and ERA5 global water vapor shows increasing trends at three pressure levels. The positive global water vapor trends from COSMIC data are 3.47±1.77, 3.25±1.25, and 2.03±0.65 %/Decade at 300, 500, and 850 hPa, respectively. The positive global water vapor trends can be the response to the global surface temperature increase (Held and Soden, 2006; Santer et al., 2006; Zhang et al., 2013; Chen and Liu, 2016; Ho et al., 2018; Allan et al., 2022).

iii)   The latitude-mean water vapor trends are mostly positive (increasing) except in the southern -80º to -60º latitude zone and have substantial variabilities (between 0.4 to ~6 %/Decade) with latitude bins. The trend difference between COSMIC and ERA5 is less than 2 %/Decade for most latitude bins at three pressure levels.

iv)   The regional distribution of water vapor trends in the tropical and subtropical regions has large local variabilities and is mixed with strong increasing and decreasing slopes. The regions in the equatorial Pacific Ocean with strong increasing water vapor trends are identified. Negative (decreasing) water vapor trends, i.e., becoming drier, are observed near the Indo-Pacific Ocean region at 500 and 850 hPa.

710   v) The assessment of regional water vapor trend variability and consistency between COSMIC and ERA5 indicates

a) A significant difference between the water vapor trends was estimated with COSMIC and ERA5 data at 850 hPa over two stratocumulus cloud-rich ocean sites. The possible cause of smaller trends from ERA5 water vapor data over stratocumulus cloud-rich regions could be the difficulty in accurately estimating water vapor at low heights in ERA5 reanalysis data (Lonitz and Geer 2017) compared with COSMIC RO measurements
715   that are unaffected by stratocumulus cloud.

b) Over land, significantly increasing water vapor trends at 850 hPa can be observed around the region (Latitude: 35º, Longitude: 275º) in the southern United States and the region (Latitude: 25º, Longitude: 115º) near south-eastern China. Two sites in southern Africa and Australia have long-term negative water vapor trends at 850 hPa, which can cause a regional long-term drier atmosphere and intensified droughts. The site
720   in Australia has huge negative trends (< -10%/Decade at 850 hPa) (becoming drier) from both COSMIC and ERA5 water vapor trends, which is consistent with Dai (2006) and Zhang et al. (2018).

c) The differences between the water vapor trends of COSMIC and ERA5 are primarily negative in the tropical regions at 850 hPa. At 500 hPa, the negative differences are mainly distributed in the Indo-Pacific Ocean region. In contrast, the positive difference is located near its northern coast in the northern Indian Ocean.

725

From our analysis, the regions with notable trend differences between COSMIC and ERA5 are mostly distributed within the northern and southern boundary of the ITCZ area, over the Indo-Pacific warm pool or central Africa. These regions experience frequent convection, such as deep convective clouds. Because of the cloud-penetration property of GNSS signal and higher height-resolution of RO retrieval, it can be better characterized for the height and temporal distribution of water vapor in RO
730 retrievals than ERA5 in the presence of convection, such as deep clouds. The better representation of water vapor in RO data may cause the difference in water vapor trend estimation between COSMIC and ERA5 over these regions, which will need further studies with other long-term water vapor data. In particular, the comparison with long-term ground-based GNSS and GPS data (Mears et al., 2017) and radiosonde data (Patel and Kuttippurath, 2022) can help address the biases and trend differences between RO and reanalysis model over land.

735

In analyzing long-term water vapor trends from RO data, it is important to select a consistent and stable reanalysis model as the reference and apply sampling error removal to correct the biases due to the limited time and location coverage of RO data. Our study shows that the COSMIC water vapor retrievals are more consistent with ERA5 than ERA-Interim model data. The overall global water vapor trends derived in this paper are close to the trending results from Allan et al. (2022). We postulate
740 that using other global reanalysis models, such as NCEP and MERRA-2, may have compatible global trends but differ in regional trends from our results, which will need further evaluation.

The importance of applying sampling error removal in our COSMIC and ERA5 water vapor trend comparison analysis is also worth noting. The sampling error removal accounts for the difference between the orbital-specific distribution of COSMIC RO measurements and uniformly-distributed global ERA5 data. Our estimation of the reduction in uncertainty after applying sampling error removal at 500 and 850 hPa is about 4.8 and 3.1 times, respectively. This magnitude of uncertainty reduction is close to that shown by Gleisner et al. (2020).

This paper compares twelve years of COSMIC data from 2007-2018 with ERA5 reanalysis data. As the follow-on mission of COSMIC, the COSMIC-2 constellation with six satellites has continued to produce RO data since 2019 (Ho et al., 2020b; Ho et al., 2022). In addition, commercial RO sensors such as Spire and GeoOptics (Chen et al., 2021) and the upcoming RO sensors onboard MetOp Second Generation and other RO missions continue to augment the temporal and spatial coverage of RO data. These growing RO datasets combined with the historical multiple RO mission data will provide the opportunity to establish consistent long-term CDR-grade global temperature, water vapor, and derived climatology data products. It is important to emphasize that consistently processed temperature and water vapor data with the same excess phase to bending angle and 1DVAR retrieval models is critical to establish such kind of long-term CDR-grade datasets from multiple RO mission data.

Appendix

1. Seasonal variability of COSMIC and ERA5 water vapor distribution

To understand the seasonal variability of water vapor at different pressure levels, we show the annual variation of mean water vapor over 12 months in eight latitudinal bins (20-degree bins from -80 to 80 degrees in latitude) in Fig. A.1a, c, e and A.2a, c, e at 300, 500, and 850 hPa pressure levels for the southern and northern hemisphere, respectively. The 12-year (2007 to 2018) water vapor data of each month and in each latitude bin have been averaged for COSMIC and ERA5. Figures A.1a, c, e, and A.2a, c, e show that the water vapor is high (wet) in the summer and low (dry) in the winter for the corresponding hemisphere at all three pressure levels. The latitudinal and seasonal variability of water vapor differences between COSMIC and ERA5 are further quantified as the relative difference ($\Delta Q_{COSMIC-ERA5}(\%)$) in Fig. A.1b, d, f and A.2b, d, f for the southern and northern hemisphere, respectively.
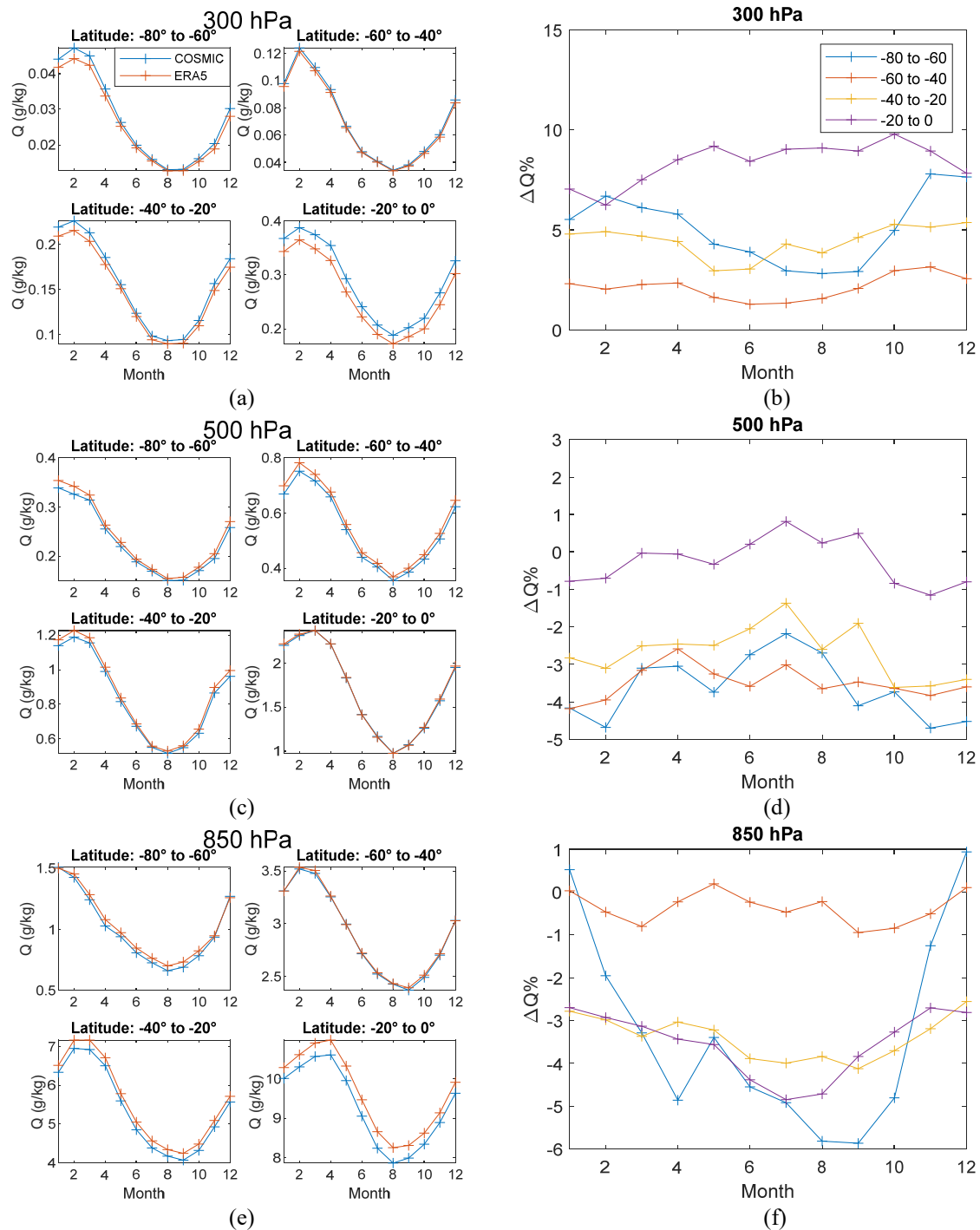
Figure A.1: (a, c, e) Comparison of seasonal variability (over 12 months) between COSMIC and ERA5 water vapor data in 4 southern hemisphere latitude bins at 300, 500, and 850 hPa, respectively. (b, d, f) Seasonal variation of the percent difference between COSMIC and ERA5 water vapor data grouped in 4 southern hemisphere latitude bins at 300, 500, and 850 hPa, respectively.

(a)

(b)

(c)

(d)

(e)

(f)
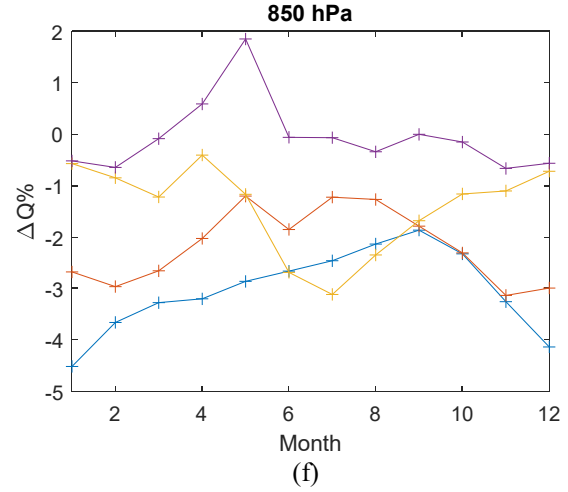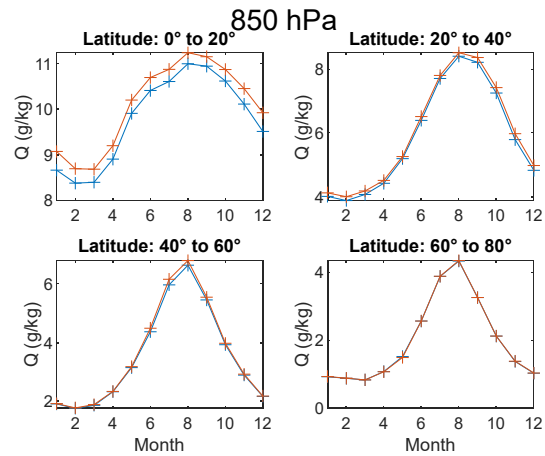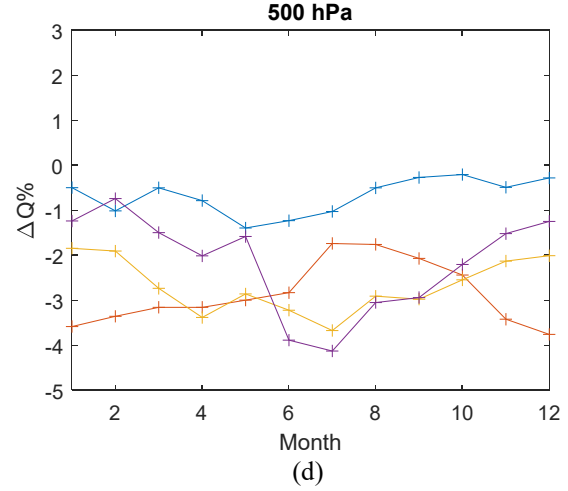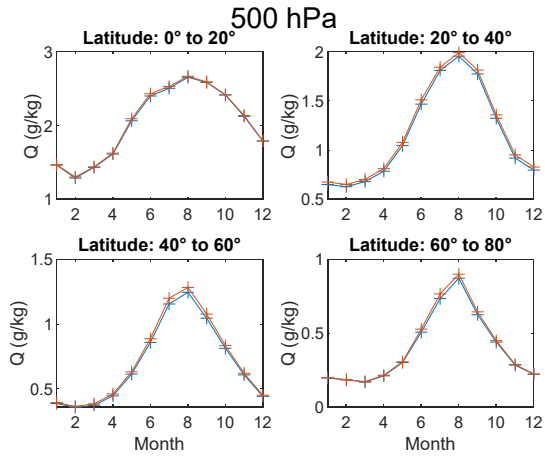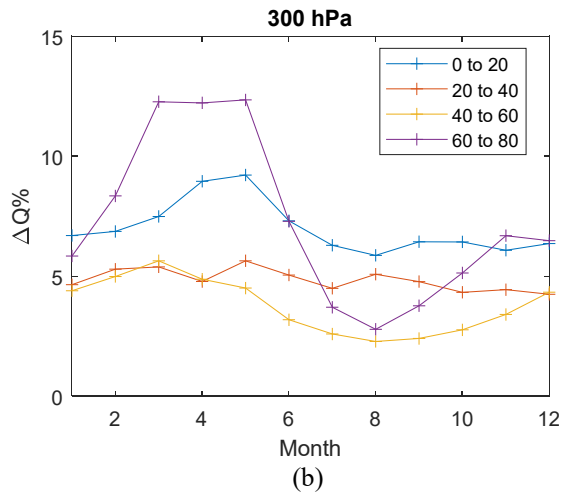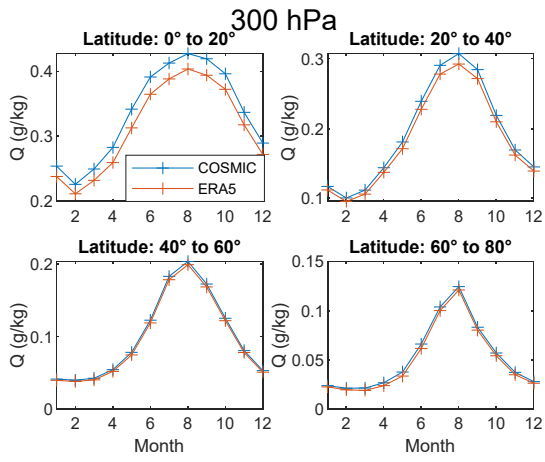
Figure A.2 Same as Fig. A.1, but over the northern hemisphere.

Figures A.1a,c,e, and A.2a,c,e show the overall agreement in seasonal variability between COSMIC and ERA5 at three pressure levels over the northern and southern hemispheres. We can use COSMIC data as a reference to evaluate the overall seasonal variability in different latitude zones. We extracted the summer maximum ($Q_{max,COSMIC}$) and winter minimum ($Q_{min,COSMIC}$) monthly mean COSMIC water vapor from Fig. A.1 and A.2. In Fig. A.3, we show the summer maximum and winter minimum monthly mean COSMIC water vapor and the annual water vapor variation magnitude defined as $\Delta Q_{max-min,COSMIC} = Q_{max,COSMIC} - Q_{min,COSMIC}$ at three pressure levels. Over all three pressure levels, the two low latitude bins (-20º to 0º and 0º to 20º) both have comparable $Q_{max,COSMIC}$, $Q_{min,COSMIC}$, and $\Delta Q_{max-min,COSMIC}$, which suggest that the mixture of water vapor in these two southern and northern latitude zones is quite efficient at all three pressure levels. As approaching higher latitudes in bins with |latitude| > 20º, the southern hemisphere atmosphere is generally drier than the matching latitude zones in the northern hemisphere at all three pressure levels. Figure A.3 also shows that the seasonal water vapor variabilities, i.e., $\Delta Q_{max-min,COSMIC}$, are more significant in the northern hemisphere than in the southern hemisphere for latitude zones above 20 degrees at all three pressure levels.

Next, we quantify the difference in the seasonal variability between the COSMIC and ERA5 water vapor data. As shown in Fig. A.1b and A.2b, at 300 hPa, $\Delta Q_{COSMIC-ERA5}(\%)$ are all positive, i.e., $Q_{COSMIC} > Q_{ERA5}$, with values ranging from 1% to 12.5% over twelve months and both hemispheres. The strongest seasonal variability in the peak-to-valley value of annual $\Delta Q_{COSMIC-ERA5}(\%)$ occurs in the northern 60º to 80º latitude bin with seasonal variation around ~8% from March to August. The high (60º to 80º) and low (0º to 20º) latitude bins in both northern and southern hemispheres all have a peak-to-valley value of annual $\Delta Q_{COSMIC-ERA5}(\%)$ higher than 4%. For middle (20º to 60º) latitude bins in northern and southern hemispheres, the magnitude of seasonal variation of $\Delta Q_{COSMIC-ERA5}(\%)$ is less than 2%. The latitudinal variability of $\Delta Q_{COSMIC-ERA5}(\%)$ agrees with the mean latitudinal values shown in Fig. 3c.

At 500 hPa, Fig. A.1d and A.2d show that $\Delta Q_{COSMIC-ERA5}(\%)$ are negative over twelve months for all latitude bins except the -20º to 0º latitude bin which has $\Delta Q_{COSMIC-ERA5}(\%)$ varying from -1% to 1%. The overall peak-to-valley seasonal variabilities of $\Delta Q_{COSMIC-ERA5}(\%)$ are in the range of 1% to 3%, with the most significant seasonal variability (~3%) in the 60º to 80º high latitude bin. Such magnitudes of seasonal variability of $\Delta Q_{COSMIC-ERA5}(\%)$ at 500 hPa are much smaller than those at 300 hPa, which suggests that using $\Delta Q_{COSMIC-ERA5}(\%)$ as the metrics, the water vapor of COSMIC retrieval is more consistent with ERA5 at 500 hPa than at 300 hPa. The latitudinal variability of $\Delta Q_{COSMIC-ERA5}(\%)$ at 500 hPa is consistent with the mean latitudinal values shown in Fig. 3f.

At 850 hPa, Fig. A.1f and A.2f show that $\Delta Q_{COSMIC-ERA5}(\%)$ are dominantly negative over twelve months for all latitude bins except one bin in latitude 60º to 80º which has $\Delta Q_{COSMIC-ERA5}(\%)$ varying from -0.7% to 1.2%. The seasonal variabilities (peak to valley variation of annual $\Delta Q_{COSMIC-ERA5}(\%)$) are weak (< 2.5%) for all of the latitude bins except the southern high

latitude bin in -80º to -60º which has the most significant seasonal variability ~ 6%. The latitudinal variability of $\Delta Q_{COSMIC-ERA5}(\%)$ at 850 hPa agrees with Fig. 3i.

825
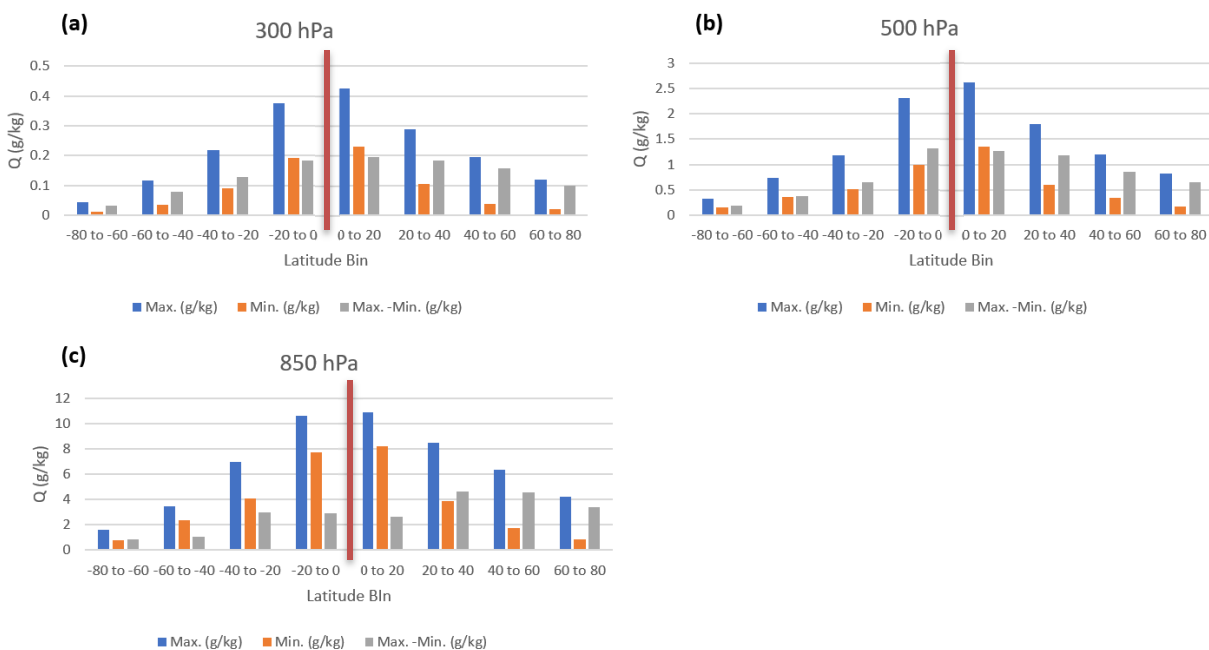
Figure A.3: Maximum, minimum, and maximum-minimum annual monthly water vapor statistics at three pressure levels (a) 300, (b) 500, and (c) 850 hPa from COSMIC retrievals. The vertical red line in each panel separates the latitude bins in the southern (to its left) and northern (to its right) hemispheres.

830 **2. Method of removing the COSMIC sampling errors for water vapor time series analysis**

The steps of calculating COSMIC sampling error and reconstructing the water vapor time series for trend analysis are detailed as follows.

 1) For a RoI such as the global, latitudinal bins, or a 10°× 10° latitude/longitude grid, the collocated water vapor data from COSMIC and ERA5 in that region are accumulated for each month. For COSMIC WETPrf data, the location of
835  the RO profile is used to determine whether the RO data is in the RoI. For a given pressure layer, interpolation over the RO profile pressure levels was carried out for COSMIC water vapor data to derive the water vapor at the specific pressure. The ERA5 data are distributed globally on 0.2-degree latitude/longitude grids, 37 pressure layers, and 6-hour intervals. Therefore, we interpolate ERA5 data over latitude/longitude and time at the given pressure level that matches the COSMIC RO observation. With the accumulated monthly COSMIC or ERA5 water vapor data for a
840  given RoI, the monthly mean values at a given pressure level are calculated to form the long-term time series of

monthly-mean water vapor ($\overline{Q_{COSMIC\_Sample}}$) for the RoI. Figure A.4a shows an example of the long-term time series of COSMIC ($\overline{Q_{COSMIC\_Sample}}$) and ERA5 ($\overline{Q_{ERA5\_Sample}}$) water vapor variation at 850 hPa pressure level for the 0°-20° latitude bin RoI in the northern hemisphere.
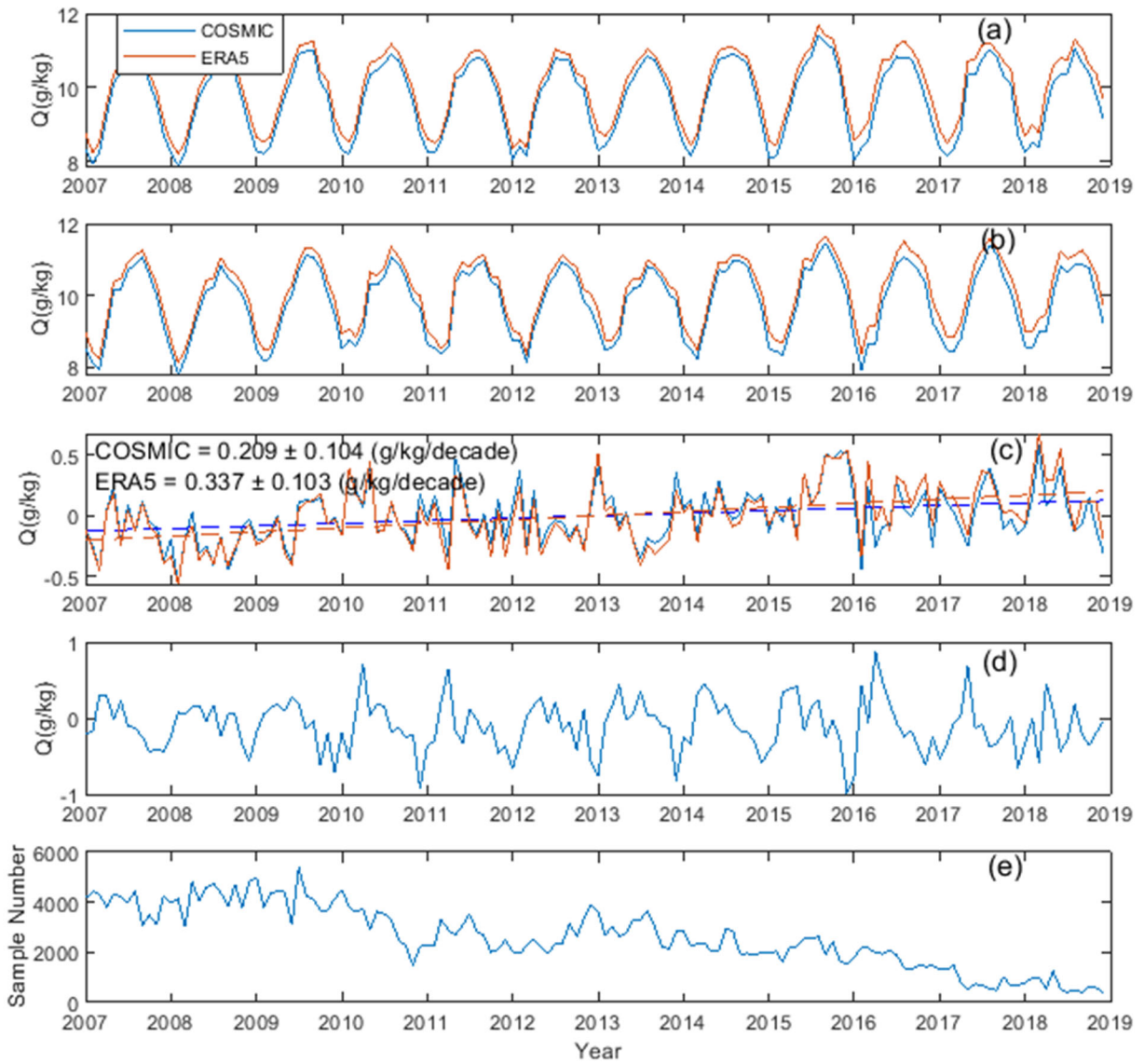
845

Figure A.4 Steps to derive the long-term water vapor trend for a given RoI at pressure level = 850 hPa. (a) The time series of the monthly mean of collocated COSMIC and ERA5 water vapor data in the 0°-20° latitude bin over the northern hemisphere. (b) Time series of COSMIC and ERA5 water vapor data after sampling error removal. (c) The deseasonalized monthly-mean COSMIC and ERA5 water vapor data time series over the 0°-20° latitude bin. Dashed lines are the trends derived from linear
850 **regression. In (a-c), red and blue lines are time series of ERA5 and COSMIC water vapor data or trends, respectively. (d) Time series of COSMIC water vapor sampling error Q_{SE} calculated with Eq. (A.1). (e) The sample number of COSMIC observations time series fall into the 0° -20° latitude bin.**

2) Fig. A.4e shows the monthly sample number of COSMIC RO data that fall into the 0˚-20˚ latitude bin RoI and has substantial variations over the lifetime of COSMIC when the number of available RO sensors in the COSMIC constellation varies over time. Particularly, there was a continuous decrease in the sample number after the middle of 2013. There are six small satellites (C1E1 to C1E6) in COSMIC-1 constellation. The service interval and performance of these six satellites vary over time. C1E3 is the first satellite that stopped producing data in the middle of 2010. C1E2, C1E3 and C1 E4 ended their operations over the time interval from 2015 to 2017. C1E1 and C1E6 continued in operation until the middle of 2019 and early 2020, respectively. Due to the varying performances and availabilities of C1E1 to C1E6, the time series of the combined valid profile numbers from these six satellites thus show the pattern shown in Fig. A.4e.

To account for the impacts of the limited and varying sample number on the trending analysis, we need to apply sampling error removal to COSMIC data. The sampling errors are the difference between the sample-mean and cell-mean, which can be estimated using monthly ERA5 data from 2007 to 2018. Eq. (A.1) illustrates the calculation of the sampling error (Q_{SE}).

$$Q_{SE} = \overline{Q_{ERA5\_Sample}} - \overline{Q_{ERA5\_RoI}}, \qquad\qquad (A.1)$$

where $\overline{Q_{ERA5\_Sample}}$ is the monthly mean of the interpolated water vapor profiles from ERA5 that match the COSMIC RO observations in the RoI at a given pressure level; $\overline{Q_{ERA5\_RoI}}$ is the monthly spatial and temporal mean of the ERA5 water vapor in the RoI at the same pressure level. The sampling error removal is carried out by subtracting monthly Q_{SE} from the COSMIC monthly water vapor data using Eq. (A.2)

$$Q_{COSMIC\_SER} = \overline{Q_{COSMIC\_Sample}} - Q_{SE}, \qquad\qquad (A.2)$$

where Q_{COSMIC_SER} is the COSMIC water vapor data after sampling error removal. For ERA5 data, the application of sampling error Q_{SE} removal to $\overline{Q_{ERA5\_sample}}$ essentially recovers $\overline{Q_{ERA5\_RoI}}$. The time series of Q_{COSMIC_SER} are unaffected by the limited and varying sample number of COSMIC RO observations. They are used to construct monthly-mean climatology (MMC) water vapor data records and characterize the long-term trend of water vapor variation for a given RoI. Fig. A.4b compares the time series of Q_{COSMIC_SER} and $\overline{Q_{ERA5\_RoI}}$ for the 0˚-20˚ latitude bin RoI at 850 hPa.

Fig. A.4d shows the time series of COSMIC sampling error Q_{SE} in the 0˚-20˚ latitude bin. Similar to the COSMIC sampling error data shown in Gleisner et al. (2020) and Shen et al. (2021), there are seasonal oscillations (around 0

g/kg) in the time series of water vapor sampling error shown in Fig. A.4d, which is mainly due to the difference between the orbital-specific distribution of COSMIC RO observations (Ho et al., 2020a) and uniformly-distributed global ERA5 data. The non-uniform local time and latitude distribution of COSMIC-1 profiles coupled with the annual variation of the Sun's declination contribute to the seasonal oscillation in the sampling error time series. As the monthly sample number of COSMIC RO data decreases after 2010 (Fig. A.4e), Q_{SE} appears to have increased amplitudes. Over the interval after the middle of 2017, when the sample number of COSMIC decreases more significantly, Q_{SE} appears to have more rapid oscillations.

3) As shown in Fig. A.4b, there are substantial seasonal oscillations in the monthly-mean water vapor data time series after the sampling error removal. To calculate the long-term trend from the time series data, the monthly mean water vapor data must be deseasonalized to filter out the annual oscillation. This step is carried out by grouping the monthly-mean water vapor data of the same month over the 2007-2018 period and calculating the mean as climate monthly mean. In this way, we have twelve monthly climate water vapor means that can characterize the annual water vapor variation. The long-term water vapor time series is then deseasonalized by subtracting the corresponding climate monthly mean at each data point. Figure A.4c shows an example of the time series of the deseasonalized water vapor for COSMIC and ERA5 at 850 hPa pressure level in the 0° -20° latitude bin RoI.

4) Linear regression has been carried out with the deseasonalized time series of water vapor to calculate the slope, i.e., the trend D_Q (g/kg/decade), of the water vapor variation. The example in Fig. A.4c shows the linear fitting curves as dashed red and blue lines for ERA5 and COSMIC data, respectively. The values and 95% confidence interval of the ERA5 and COSMIC water vapor trends are also listed in the figure.

3. Effects of sampling error removal on the uncertainty of the regional water vapor trend analysis

Figure A.5a and b show the global (10°×10°) distribution of trends derived from the sampling error Q_{SE} time series at 500 and 850 hPa, respectively. The grids with > 1.5% missing monthly data over the 2007 to 2018 interval are marked as white blanks in Fig. A.5a and A.5b. It can be seen that the sampling error removal does introduce corrections to the regional trends of COSMIC water vapor data. To further evaluate the impacts of the sampling error removal on the uncertainty of the water vapor trend analysis using long-term COSMIC water vapor data, we calculated the histogram distribution of the relative water vapor trend difference between the COSMIC and ERA5 data, i.e., $\Delta ND_Q = ND_{Q,COSMIC} - ND_{Q,ERA5}$, from the global (10°×10°) distribution. In particular, COSMIC water vapor data without and with sampling error removal are used to calculate $\Delta ND_{Q,without\ SER}$ and $\Delta ND_{Q,with\ SER}$, respectively. Fig. A.6a and b show the histogram distribution and Gaussian-fit of $\Delta ND_{Q,without\ SER}$ and $\Delta ND_{Q,with\ SER}$ at 500 and 850 hPa, respectively. Gleisner et al. (2020) showed that removing sampling error could help reduce the uncertainty to about 1/3 in analyzing multiple RO data products processed by RO Meteorology Satellite Application Facility (ROM SAF). From our analysis, the Full-Width-Half-Maximum (FWHM) histogram distribution

in Fig. A.6a and b has been reduced from 28.1%/Decade and 25.6%/Decade to 5.8%/Decade and 8.2%/Decade at 500 and 850 hPa, respectively, after applying the sampling error removal to COSMIC data. This is about a 4.8 and 3.1-time reduction in uncertainty at 500 and 850 hPa, respectively, which is quite close to the ~3 times of uncertainty reduction shown in Gleisner et al. (2020). We note that the ERA5 trending is used as the reference in the uncertainty analysis. On the other hand, the remaining differences between $ND_{Q,COSMIC}$ with sampling error removal and $ND_{Q,ERA5}$ can be partly due to better cloud-penetration characteristics of COSMIC RO observations over regions with frequent clouds. Therefore, our analysis of the impacts of sampling error removal on trend uncertainty provides an upper-bound estimation.

(a)   (b)
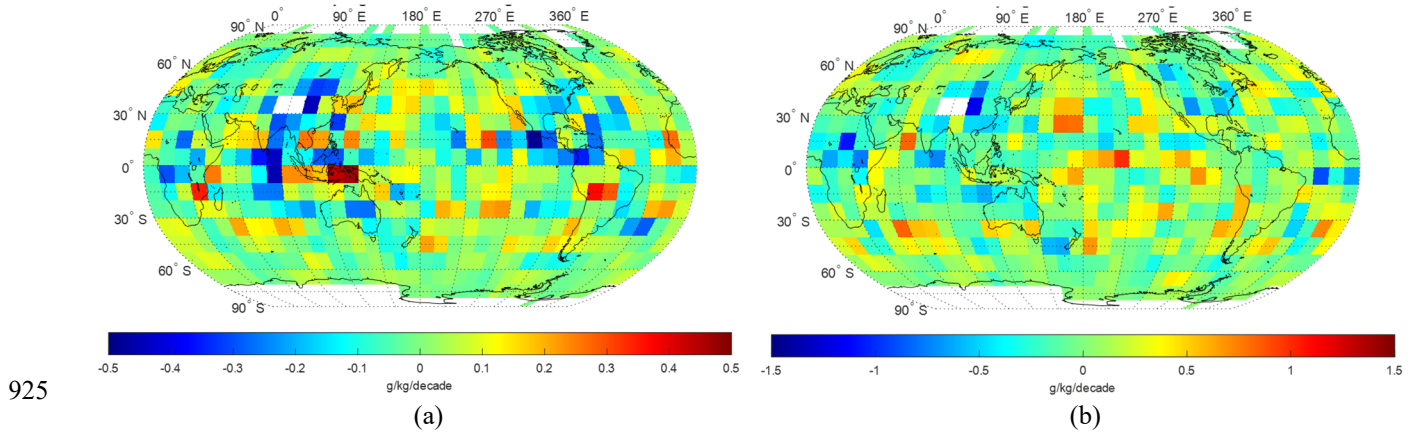
Figure A.5: (a) and (b) The distribution of trends of sampling error Q_{SE} time series at 500 and 850 hPa, respectively. The white blanks in (a) and (b) are grids with > 1.5% missing monthly data over the 2007 to 2018 interval.

(a)   (b)
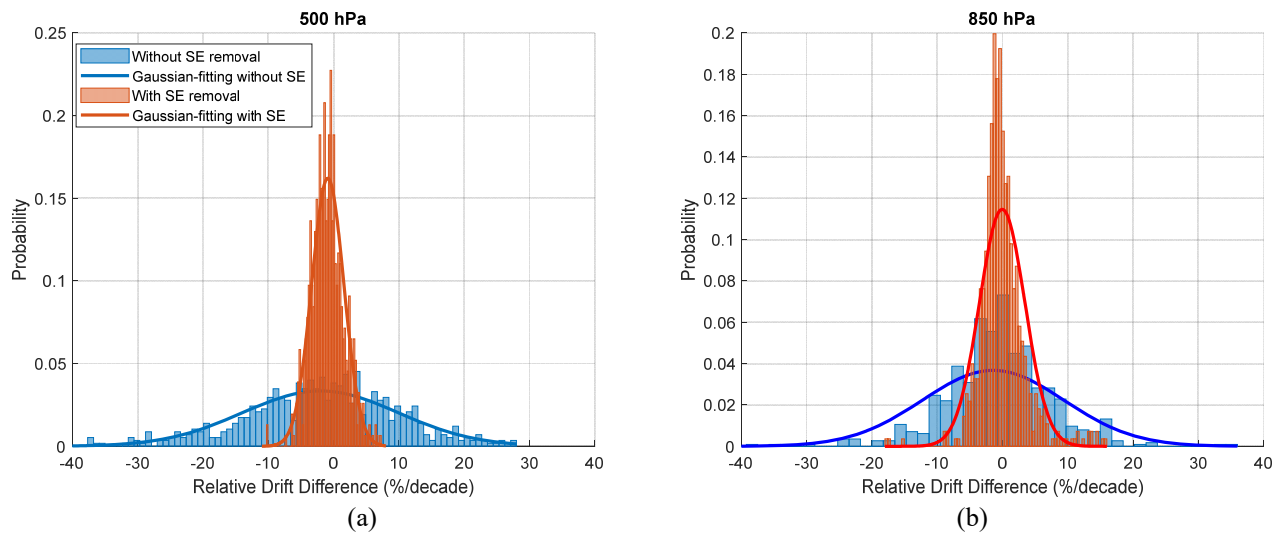
Figure A.6: (a, b) The histogram distributions of relative water vapor trend difference (%/decade) between COSMIC and ERA5 water vapor at 500 and 850 hPa, respectively. In both panels, blue and orange bar charts are the distribution of the COSMIC water vapor trend difference relative to ERA5 before and after the sampling error removal was applied, respectively. The blue and red lines are the Gaussian-fitted distribution of the relative water vapor trend difference for the FWHM calculation.

Data availability. The ECMWF ReAnalysis Model 5 (ERA5) data are publicly available at https://www.ecmwf.int/en/forecasts/dataset/ecmwf-reanalysis-v5. The UCAR COSMIC water vapor data are available at https://cdaac-www.cosmic.ucar.edu/cdaac/products.html.

940

Author contribution. Conceptualization by SH and XS. XS, SH, XZ, and YC defined the validation methodology. XJ, TL, XS, and BZ wrote the scripts used for the analysis. XJ, TL, XS, BZ, and JD performed the data analysis and validation. XZ, BZ, and JD provided the satellite data. XS and SH wrote the manuscript. XS, SH, XZ, YC, TL, BZ, and JD reviewed and edited the manuscript. Project administration by XS and BZ. Funding acquisition by SH and YC. All authors have read and agreed to the published version of the manuscript.

945

Competing interests. The authors declare that they have no conflict of interest.

950 Acknowledgments. The author would like to thank Guojun Gu, Yun Zhou and Loknath Adhikari for their input during the process of this manuscript. The manuscript contents are solely the opinions of the authors and do not constitute a statement of policy, decision, or position on behalf of NOAA or the U.S. government.

Financial support. This study was supported by NOAA grant NA19NES4320002 (Cooperative Institute for Satellite Earth 955 System Studies-CISESS) at the University of Maryland/ESSIC.

References

Ao, C. O., Meehan, T. K., Hajj, G. A., Mannucci, A. J., and Beyerle, G.: Lower-troposphere refractivity bias in GPS occultation retrievals, *J. Geophys. Res.*, **108**(D18), 4577, doi:10.1029/2002JD003216, 2003.

960 Ao, C. O.: Effect of ducting on radio occultation measurements: An assessment based on high-resolution radiosonde soundings, *Radio Sci.*, **42**, RS2008, doi:10.1029/2006RS003485, 2007.

Adler, R.F., Gu, G., Wang, J.J., Huffman, G.J., Curtis, S. and Bolvin, D.: Relationships between global precipitation and surface temperature on interannual and longer timescales (1979–2006). *Journal of Geophysical Research: Atmospheres*, *113*(D22)., doi:10.1029/2008JD010536, 2008.

965 Ahrens, C., and Samson, P.: Extreme Weather and Climate, 1st ed., Brooks Cole, United States of America, 2011.

Allan, R. P.: Analysis of moisture variability in the European Centre for Medium-Range Weather Forecasts 15-year reanalysis over the tropical oceans, J. Geophys. Res., 107(D15), 4230, doi:10.1029/2001JD001132, 2002.

Allan, R. P., & Soden, B. J.: Atmospheric warming and the amplification of precipitation extremes. Science, 321(5895), 1481-1484, DOI: 10.1126/science.1160787, 2008.

970 Allan, R. P., & Liepert, B. G.: Anticipated changes in the global atmospheric water cycle. Environmental Research Letters, 5(2), 025201, DOI:10.1088/1748-9326/5/2/025201, 2010.

Allan, R. P., Liu, C., Zahn, M., Lavers, D. A., Koukouvagias, E., & Bodas-Salcedo, A.: Physically consistent responses of the global atmospheric hydrological cycle in models and observations. Surveys in Geophysics, 35(3), 533-552, DOI:10.1007/s10712-012-9213-z, 2014.

975 Allan, R. P., Willett, K. M., John, V. O., & Trent, T.: Global changes in water vapor 1979–2020. *Journal of Geophysical Research: Atmospheres*, 127, e2022JD036728, doi.org/10.1029/2022JD036728, 2022.

Alley, R., Berntsen, T., Bindoff, N.L., Chen, Z., Chidthaisong, A., Friedlingstein, P., Gregory, J., Hegerl, G., Heimann, M., Hewitson, B. and Hoskins, B.: Climate change 2007: The physical science basis. *Contribution of Working Group I to the Fourth Assessment Report of the Intergovernmental Panel on Climate Change. Summary for Policymakers. IPCC*
980 *Secretariat, Geneva, Switzerland. 21p, 2007.*

Andrisaniand, A., & Vespe, F.: Humidity profiles retrieved from GNSS Radio Occultations by a non-negative residual constrained least square error method. *Frontiers in Earth Science*, 320, DOI: 10.3389/feart.2020.00320, 2020.

Anthes, R. A., Rocken, C., & Ying-Hwa, K.: Applications of COSMIC to meteorology and climate. *Terr. Atmos. Oceanic Sci.,* **11**, 115-156, DOI: 10.3319/TAO.2000.11.1.115(COSMIC), 2020.

985 Anthes, R.A., Bernhardt, P.A., Chen, Y., Cucurull, L., Dymond, K.F., Ector, D., Healy, S.B., Ho, S.P., Hunt, D.C., Kuo, Y.H. and Liu, H.,: The COSMIC/FORMOSAT-3 mission: Early results. *Bulletin of the American Meteorological Society*, *89*(3), pp.313-334., DOI: 10.1175/BAMS-89-3-313, 2008.

Bengtsson, L.: Can climate trends be calculated from reanalysis data?, J. Geophys. Res., 109, D11111, DOI:10.1029/2004JD004536, 2004.

990 Bock, O., Guichard, F., Janicot, S., Lafore, J. P., Bouin, M. N., & Sultan, B.: Multiscale analysis of precipitable water vapor over Africa from GPS data and ECMWF analyses, Geophys. Res. Lett., 34, L09705, DOI:10.1029/2006GL028039, 2007.

Borger, C., Beirle, S., & Wagner, T.: A 16-year global climate data record of total column water vapour generated from OMI observations in the visible blue spectral range. *Earth System Science Data Discussions*, 1-25, DOI:10.5194/essd-2021-319, 2021.

995 Chen Y, Shao X, Cao C, Ho S-P.: Simultaneous Radio Occultation Predictions for Inter-Satellite Comparison of Bending Angle Profiles from COSMIC-2 and GeoOptics. *Remote Sensing*. 13(18):3644. https://doi.org/10.3390/rs13183644, 2021.

Chen Y, Cao C, Shao X, Ho S-P.: Assessment of the Consistency and Stability of CrIS Infrared Observations Using COSMIC-2 Radio Occultation Data over Ocean. *Remote Sensing*, 14(11):2721. DOI:10.3390/rs14112721, 2022.

Chen, B., & Liu, Z.: Global water vapor variability and trend from the latest 36 year (1979 to 2014) data of ECMWF and
1000 NCEP reanalyses, radiosonde, GPS, and microwave satellite. *Journal of Geophysical Research: Atmospheres*, *121*(19), 11-442, DOI:10.1002/2016JD024917, 2016.

Chou, C., & Neelin, J. D.: Mechanisms of global warming impacts on regional tropical precipitation. Journal of climate, 17(13), 2688-2701, https://doi.org/10.1175/JCLI-D-11-00239.1, 2004.

Dai, A.: Recent climatology, variability, and trends in global surface humidity, J. Clim., 19(15), 3589–3606, DOI:10.1175/JCLI3816.1, 2006.

De Deckker, P.: The Indo-Pacific Warm Pool: critical to world oceanography and world climate. Geoscience Letters, 3(1), 1-12, DOI:10.1186/s40562-016-0054-3, 2016.

Feulner, G., Rahmstorf, S., Levermann, A., & Volkwardt, S.: On the Origin of the Surface Air Temperature Difference between the Hemispheres in Earth's Present-Day Climate, Journal of Climate, 26(18), 7136-7150, DOI:10.1175/JCLI-D-12-00636.1, 2013.

Fujiwara, M., Wright, J. S., Manney, G. L., Gray, L. J., Anstey, J., Birner, T., Davis, S., Gerber, E. P., Harvey, V. L., Hegglin, M. I., Homeyer, C. R., Knox, J. A., Krüger, K., Lambert, A., Long, C. S., Martineau, P., Molod, A., Monge-Sanz, B. M., Santee, M. L., Tegtmeier, S., Chabrillat, S., Tan, D. G. H., Jackson, D. R., Polavarapu, S., Compo, G. P., Dragani, R., Ebisuzaki, W., Harada, Y., Kobayashi, C., McCarty, W., Onogi, K., Pawson, S., Simmons, A., Wargan, K., Whitaker, J. S., and Zou, C.-Z.: Introduction to the SPARC Reanalysis Intercomparison Project (S-RIP) and overview of the reanalysis systems, Atmos. Chem. Phys., 17, 1417–1452, https://doi.org/10.5194/acp-17-1417-2017, 2017.

Gleisner, H., Lauritsen, K. B., Nielsen, J. K., and Syndergaard, S.: Evaluation of the 15-year ROM SAF monthly mean GPS radio occultation climate data record, Atmos. Meas. Tech., 13, 3081–3098, DOI:/10.5194/amt-13-3081-2020, 2020.

Gleisner, H., Ringer, M. A., & Healy, S. B.: Monitoring global climate change using GNSS radio occultation. *npj Climate and Atmospheric Science*, *5*(1), 1-4, DOI: 10.1038/s41612-022-00229-7, 2022.

Grossi, M., Valks, P., Loyola, D., Aberle, B., Slijkhuis, S., Wagner, T., Beirle, S., and Lang, R.: Total column water vapour measurements from GOME-2 MetOp-A and MetOp-B, Atmospheric Measurement Techniques, 8, 1111–1133, DOI: 10.5194/amt-8-1111-2015, 2015.

Gu, G., and Adler, R. F.: Interdecadal Variability/Long-Term Changes in Global Precipitation Patterns during the Past Three Decades: Global Warming and/or Pacific Decadal Variability? *Clim. Dyn.*, 40, 3009-3022., doi: 10.1007/s00382-012-1443-8, 2013.

Gu, G., and Adler, R. F.: Observed Variability and Trends in Global Precipitation During 1979-2020. *Clim. Dyn.*, https://doi.org/10.1007/s00382-022-06567-9, 2022.

He, J., Brogniez, H., & Picon, L.: Evaluation of tropical water vapor from CMIP6 GCMs using the ESA CCI" Water Vapour" climate data records. *Atmospheric Chemistry and Physics Discussions*, 1-20, DOI: 10.5194/acp-2021-976, 2022.

Held, I. M., & Soden, B. J.: Water vapor feedback and global warming. Annual review of energy and the environment, 25(1), 441-475, DOI: 10.1146/annurev.energy.25.1.441, 2000.

Held, I.M. and Soden, B.J.: Robust responses of the hydrological cycle to global warming, J. Clim., 19(21), 5686–5699, DOI: 10.1175/JCLI3990.1, 2006.

1035   Hegerl, G.C., Black, E., Allan, R.P., Ingram, W.J., Polson, D., Trenberth, K.E., Chadwick, R.S., Arkin, P.A., Sarojini, B.B., Becker, A. and Dai, A.: Challenges in quantifying changes in the global water cycle. Bulletin of the American Meteorological Society, 96(7), pp.1097-1115, DOI: 10.1175/BAMS-D-13-00212.1, 2015.

Hersbach, H., Bell, B., Berrisford, P., Hirahara, S., Horányi, A., Muñoz-Sabater, J., Nicolas, J., Peubey, C., Radu, R., Schepers, D. and Simmons, A.: The ERA5 global reanalysis. *Quarterly Journal of the Royal Meteorological Society*, *146*(730),
1040   pp.1999-2049, DOI: 10.1002/qj.3803, 2020.

Ho, S.P., Kirchengast, G., Leroy, S., Wickert, J., Mannucci, A.J., Steiner, A., Hunt, D., Schreiner, W., Sokolovskiy, S., Ao, C. and Borsche, M.: Estimating the uncertainty of using GPS radio occultation data for climate monitoring: Intercomparison of CHAMP refractivity climate records from 2002 to 2006 from different data centers. *Journal of Geophysical Research: Atmospheres*, *114*(D23), DOI: 10.1029/2009JD011969, 2009.

1045   Ho, S.P., Zhou, X., Kuo, Y.H., Hunt, D. and Wang, J.H.: Global evaluation of radiosonde water vapor systematic biases using GPS radio occultation from COSMIC and ECMWF analysis. *Remote Sensing*, *2*(5), pp.1320-1330, DOI: 10.3390/rs2051320, 2010.

Ho, S.-P., Peng, L., Anthes, R. A., Kuo, Y.-H., and Lin, H.-C.: Marine boundary layer heights and their longitudinal, diurnal, and interseasonal variability in the southeastern Pacific using COSMIC, CALIOP, and radiosonde data. *J. Climate*, **28**,
1050   2856–2872, doi.org/10.1175/JCLI-D-14-00238.1, 2015.

Ho, S. P., Peng, L., Mears, C., & Anthes, R. A.: Comparison of global observations and trends of total precipitable water derived from microwave radiometers and COSMIC radio occultation from 2006 to 2013. *Atmospheric Chemistry and Physics*, *18*(1), 259-274, DOI: 10.5194/acp-18-259-2018, 2018.

Ho, S.P., Anthes, R.A., Ao, C.O., Healy, S., Horanyi, A., Hunt, D., Mannucci, A.J., Pedatella, N., Randel, W.J., Simmons, A.
1055   and Steiner, A.: The COSMIC/FORMOSAT-3 radio occultation mission after 12 years: Accomplishments, remaining challenges, and potential impacts of COSMIC-2. *Bulletin of the American Meteorological Society*, *101*(7), pp.E1107-E1136., doi:10.1175/BAMS-D-18-0290.1, 2020a.

Ho, S.P., Zhou, X., Shao, X., Zhang, B., Adhikari, L., Kireev, S., He, Y., Yoe, J.G., Xia-Serafino, W. and Lynch, E.: Initial assessment of the COSMIC-2/FORMOSAT-7 neutral atmosphere data quality in NESDIS/STAR using in situ and satellite
1060   data. *Remote Sensing*, *12*(24), p.4099, DOI: 10.3390/rs12244099, 2020b.

Ho S-p, Kireev S, Shao X, Zhou X, Jing X.: Processing and Validation of the STAR COSMIC-2 Temperature and Water Vapor Profiles in the Neutral Atmosphere. *Remote Sensing*., 14(21):5588, doi.org/10.3390/rs14215588, 2022.

Huang, C.Y., Teng, W.H., Ho, S.P. and Kuo, Y.H.: Global variation of COSMIC precipitable water over land: Comparisons with ground-based GPS measurements and NCEP reanalyses. *Geophysical Research Letters*, *40*(19), pp.5327-5331, DOI:
1065   10.1002/grl.50885, 2013.

Iacovazzi, R., Lin, L., Sun, N. and Liu, Q.: NOAA operational microwave sounding radiometer data quality monitoring and anomaly assessment using COSMIC GNSS radio-occultation soundings. *Remote Sensing*, *12*(5), p.828. DOI: 10.3390/rs12050828, 2020.

Johnston, B.R., Randel, W.J., Sjoberg J.P.: Evaluation of Tropospheric Moisture Characteristics Among COSMIC-2, ERA5 and MERRA-2 in the Tropics and Subtropics. *Remote Sensing*. 13(5), 880, DOI: 10.3390/rs13050880, 2021.

Johnston, B. R., Randel, W. J., and Braun, J. J.: Interannual Variability of Tropospheric Moisture and Temperature and Relationships to ENSO Using COSMIC-1 GNSS-RO Retrievals. *J. Climate*, **35**, 3509–3525, doi.org/10.1175/JCLI-D-21-0884.1, 2022.

Kiehl, J. T., & Trenberth, K. E.: Earth's annual global mean energy budget. Bulletin of the American meteorological society, 78(2), 197-208, DOI: 10.1175/1520-0477, 1997.

Sherwood, S.C., Roca, R., Weckwerth, T.M. and Andronova, N.G.: Tropospheric water vapor, convection, and climate. *Reviews of Geophysics*, *48*(2), DOI: 10.1029/2009RG000301, 2010.

Kursinski, E. R., Hajj, G. A., Schofield, J. T., Linfield, R. P., and Hardy, K. R.: Observing Earth's atmosphere with radio occultation measurements using the Global Positioning System, Journal of Geophysical Research: Atmospheres, 102, 23 429–23 465, https://doi.org/10.1029/97JD01569, 1997.

Kursinski, E.R. and Hajj, G.A.: A comparison of water vapor derived from GPS occultations and global weather analyses. *J. Geoph. Res.,* **106,** 1113-1138, doi: 10.1029/2000JD900421, 2021.

Lonitz, K., and Geer, A.: Effect of assimilating microwave imager observations in the presence of a model bias in marine stratocumulus, EUMETSAT/ECMWF Fellowship Programme Research Reports, https://www.ecmwf.int/node/17164, 2017.

Lu, N., Qin, J., Gao, Y., Yang, K., Trenberth, K.E., Gehne, M. and Zhu, Y.: Trends and variability in atmospheric precipitable water over the Tibetan Plateau for 2000–2010. *International Journal of Climatology*, *35*(7), pp.1394-1404. doi:10.1002/joc.4064, 2015.

Mears, C., Ho, S. P., Wang, J., Huelsing, H., and Peng, L.: Total column water vapor [in "States of the Climate in 2016"]. *Bull. Amer. Meteor. Soc.*, **98** (8), S24–S25, https://doi.org/10.1175/2017BAMSStateoftheClimate.1, 2017.

Mears, C., Ho, S.-P., Zhang, L., and Zhou, X.: Total Column Water Vapor section, in "States of the Climate in 2021". Bul. Amer. Meteor. Sci., submitted, 2002.

Mieruch, S., Noël, S., Bovensmann, H. and Burrows, J.P.: Analysis of global water vapour trends from satellite measurements in the visible spectral range. *Atmospheric Chemistry and Physics*, *8*(3), pp.491-504, doi: doi.org/10.5194/acp-8-491-2008, 2008.

Mieruch, S., Schröder, M., Noël, S. and Schulz, J., Comparison of decadal global water vapor changes derived from independent satellite time series, J. Geophys. Res. Atmos., 119, 12,489–12,499, doi:10.1002/2014JD021588, 2014.

Nilsson, T. and Elgered, G.: Long-term trends in the atmospheric water vapor content estimated from ground-based GPS data. *Journal of Geophysical Research: Atmospheres*, *113*(D19). doi:10.1029/2008JD010110, 2008.

Parker, D., Folland, C., Scaife, A., Knight, J., Colman, A., Baines, P. and Dong, B.: Decadal to multidecadal variability and the climate change background. Journal of Geophysical Research: Atmospheres, 112(D18)., doi:10.1029/2007JD008411, 2007.

Patel, V., and Kuttippurath, J.: Significant increase in water vapour over India and Indian Ocean: Implications for tropospheric warming and regional climate forcing, Science of Total Environment, https://doi.org/10.1016/j.scitotenv.2022.155885, 08, 2022.

Rosenkranz, P. W.: Retrieval of temperature and moisture profiles from AMSU-A and AMSU-B measurements, IEEE Transactions on Geoscience and Remote Sensing, 39, 2429–2435, doi: 10.1109/36.964979, 2001.

Ross, R.J. and Elliott, W.P.: Radiosonde-based Northern Hemisphere tropospheric water vapor trends. *Journal of Climate*, *14*(7), pp.1602-1612. Doi: 10.1175/1520-0442, 2001.

Santer, B.D., Wigley, T.M.L., Gleckler, P.J., Bonfils, C., Wehner, M.F., AchutaRao, K., Barnett, T.P., Boyle, J.S., Brüggemann, W., Fiorino, M. and Gillett, N.: Forced and unforced ocean temperature changes in Atlantic and Pacific tropical cyclogenesis regions. *Proceedings of the National Academy of Sciences*, *103*(38), pp.13905-13910.DOI: 10.1073/pnas.0602861103, 2006.

Sherwood, S.C., Roca, R., Weckwerth, T.M. and Andronova, N.G.: Tropospheric water vapor, convection, and climate. *Reviews of Geophysics*, *48*(2). doi:10.1029/2009RG000301, 2010.

Shao, X., Ho, S.P., Zhang, B., Cao, C. and Chen, Y.: Consistency and Stability of SNPP ATMS Microwave Observations and COSMIC-2 Radio Occultation over Oceans. Remote Sensing, 13(18), p.3754. DOI: 10.3390/rs13183754, 2021a.

Shao, X., Ho, S.P., Zhang, B., Zhou, X., Kireev, S., Chen, Y. and Cao, C.: Comparison of COSMIC-2 radio occultation retrievals with RS41 and RS92 radiosonde humidity and temperature measurements. *Terrestrial, Atmospheric & Oceanic Sciences*, *32*. doi: 10.3319/TAO.2021.12.30.02, 2021b.

Shen, Z., Zhang, K., He, Q., Wan, M., Li, L., and Wu, S.: Quest over the Sampling Error of COSMIC Radio Occultation Temperature Climatologies, *Journal of Atmospheric and Oceanic Technology*, *38*(3), 441-458. DOI:10.1175/JTECH-D-19-0169.1, 2021.

Sokolovskiy, S.: Effect of superrefraction on inversions of radio occultation signals in the lower troposphere, *Radio Sci.*, 38, 1058, doi:10.1029/2002RS002728, 2003.

Smith, T.M. and Reynolds, R.W.: A global merged land–air–sea surface temperature reconstruction based on historical observations (1880–1997). *Journal of climate*, *18*(12), pp.2021-2036. DOI: 10.1175/JCLI3362.1, 2005.

Trenberth, K. E.: Changes in precipitation with climate change. Climate research, 47(1-2), 123-138. DOI: 10.3354/cr00953, 2011.

Sun, B., Reale, T., Schroeder, S., Pettey, M. and Smith, R.: On the accuracy of Vaisala RS41 versus RS92 upper-air temperature observations. *Journal of Atmospheric and Oceanic Technology*, *36*(4), pp.635-653, doi: 10.1175/JTECH-D-18-0081.1, 2019.

Susskind, J., Barnet, C., and Blaisdell, J.: Retrieval of atmospheric and surface parameters from AIRS/AMSU/HSB data in the presence of clouds, IEEE Transactions on Geoscience and Remote Sensing, 41, 390–409, https://doi.org/10.1109/TGRS.2002.808236, 2003.

Trenberth K.E., Fasullo, J., and Smith, J.: Trends and variability in column-integrated atmospheric water vapor. Clim. Dyn., doi:10.1007/s00382-005-0017-4, 2005.

Vey, S., Dietrich, R., Rülke, A., Fritsche, M., Steigenberger, P. and Rothacher, M.: Validation of precipitable water vapor within the NCEP/DOE Reanalysis using global GPS observations from one decade, J. Clim., 23(7), 1675–1695, doi:10.1175/2009JCLI2787.1, 2010.

Wagner, T., Beirle, S., Grzegorski, M. and Platt, U.: Global trends (1996–2003) of total column precipitable water observed by Global Ozone Monitoring Experiment (GOME) on ERS-2 and their relation to near-surface temperature, J. Geophys. Res., 111, D12102, doi:10.1029/ 2005JD006523, 2006.

Wang, R., Fu, Y., Xian, T., Chen, F., Yuan, R., Li, R. and Liu, G.: Evaluation of atmospheric precipitable water characteristics and trends in mainland China from 1995 to 2012. *Journal of Climate*, *30*(21), pp.8673-8688. DOI: 10.1175/JCLI-D-16-0433.1, 2017.

Wee, T.-K.; Anthes, R.A.; Hunt, D.C.; Schreiner, W.S.; Kuo, Y.-H. Atmospheric GNSS RO 1D-Var in Use at UCAR: Description and Validation. *Remote Sens.*, *14*, 5614. DOI: 10.3390/rs14215614, 2022.

Whitaker, J. S., Hamill, T. M., Wei, X., Song, Y., & Toth, Z.: Ensemble Data Assimilation with the NCEP Global Forecast System, *Monthly Weather Review*, *136*(2), 463-482, DOI: 10.1175/2007MWR2018.1, 2008.

Wood, R., Mechoso, C. R., Bretherton, C. S., Weller, R. A., Huebert, B., Straneo, F., Albrecht, B. A., Coe, H., Allen, G., Vaughan, G., Daum, P., Fairall, C., Chand, D., Gallardo Klenner, L., Garreaud, R., Grados, C., Covert, D. S., Bates, T. S., Krejci, R., Russell, L. M., de Szoeke, S., Brewer, A., Yuter, S. E., Springston, S. R., Chaigneau, A., Toniazzo, T., Minnis, P., Palikonda, R., Abel, S. J., Brown, W. O. J., Williams, S., Fochesatto, J., Brioude, J., and Bower, K. N.: The VAMOS Ocean-Cloud-Atmosphere-Land Study Regional Experiment (VOCALS-REx): goals, platforms, and field operations, Atmos. Chem. Phys., 11, 627–654, https://doi.org/10.5194/acp-11-627-2011, 2011.

Wood, R.: Stratocumulus clouds. Mon. Wea. Rev., 140, 2373– 2423, doi:10.1175/MWR-D-11-00121.1, 2012.

Xie, F.; Syndergaard, S.; Kursinski, E. R.; Herman, B. M.: An Approach for Retrieving Marine Boundary Layer Refractivity from GPS Occultation Data in the Presence of Superrefraction, *J. Atmos. Ocean. Technol.*, *23*, 1629–1644, doi.org/10.1175/jtech1996.1, 2006.

Xie, F., Wu, D.L., Ao, C.O., Kursinski, E.R., Mannucci, A.J., Syndergaard, S.: Super-refraction effects on GPS radio occultation refractivity in marine boundary layers. *Geophys. Res. Lett.*, *37*, doi.org/10.1029/2010gl043299, 2010.

Xie, F., Tian, W., Zhou, X., Zhang, J., Xia, Y., & Lu, J.: Increase in lower stratospheric water vapor in the past 100 years related to tropical Atlantic warming. Geophysical Research Letters, 47(22), e2020GL090539, doi: 10.1029/2020GL090539, 2020.

Yadav, R., Giri, R. K., & Singh, V.: Intercomparison review of IPWV retrieved from INSAT-3DR sounder, GNSS and CAMS reanalysis data. *Atmospheric Measurement Techniques*, *14*(7), 4857-4877, DOI: 10.5194/amt-14-4857-2021, 2021.

Yuan, P., Van Malderen, R., Yin, X., Vogelmann, H., Awange, J., Heck, B., & Kutterer, H.: Characterizing Europe's integrated water vapor and assessing atmospheric reanalyses using more than two decades of ground-based GPS. *Atmospheric Chemistry and Physics Discussions*, 1-38. DOI: 10.5194/acp-2021-797, 2021.

Zhai, P. and Eskridge, R.E.: Atmospheric water vapor over China. *Journal of Climate*, *10*(10), pp.2643-2652, DOI: 10.1175/1520-0442, 1997.

Zhang, L., Wu, L. and Gan, B.: Modes and mechanisms of global water vapor variability over the twentieth century. *Journal of climate*, *26*(15), pp.5578-5593., doi:10.1175/JCLI-D-12-00585.1, 2013.

Zhang, Y., Xu, J., Yang, N. and Lan, P.: Variability and trends in global precipitable water vapor retrieved from COSMIC radio occultation and radiosonde observations. *Atmosphere*, *9*(5), p.174. DOI: 10.3390/atmos9050174, 2018

Zhao, T., Dai, A. and Wang, J.: Trends in tropospheric humidity from 1970 to 2008 over China from a homogenized radiosonde dataset. *Journal of Climate*, *25*(13), pp.4549-4567, doi:10.1175/JCLI-D-11-00557.1, 2012.

Zveryaev, I.I. and Allan, R. P.: Water vapor variability in the tropics and its links to dynamics and precipitation. J. Geophys. Res.-Atmos., 110, D21112, doi:10.1029/2005JD006033, 2005.